



SHARP Storage - Project no 327342



Stress drop and crustal strength evaluation

Deliverable 2.5

Organisation(s)	NORSAR
Author(s)	Bettina Goertz-Allmann, Nadege Langet and Anna Maria Dichiarante
Reviewer(s)	Daniel Roberts (Rockfield) & Tom Kettlety (University of Oxford)
Type of deliverable	Report
WP	2
Issue Date	August 2024
Document version	1

Contents

1	Stress drop analysis	4
1.1	Introduction	4
1.2	The Horda database	4
1.3	Spectral analysis	7
1.3.1	Displacement spectra	7
1.3.2	Spectral separation method	7
1.4	Moment magnitude	10
1.4.1	Method	10
1.4.2	Comparison to local magnitude	12
1.5	Source spectral analysis	12
1.6	Synthetic tests	15
1.6.1	Synthetic case I: regular station grid	16
1.6.2	Synthetic case II: real-station distribution	16
1.7	Conclusion of Horda stress drop estimation	25
2	Stress data integration	26
2.1	Introduction	26
2.2	In situ stress orientation for the Horda Platform	26
2.2.1	Existing WSM2016 in-situ stress data	27
2.2.2	Additional borehole stress observation	28
2.2.3	The updated focal mechanisms catalogue and additional moment tensor solutions	29
2.3	Data integration	30
2.4	Concluding remarks	42

About the report

This report constitutes Deliverable 2.5 of SHARP Storage and it is organised as follows: the first section focuses on estimating earthquake stress drops on the Horda Platform by expanding the event database and applying a data-driven analysis approach while the second section integrates stress data from early deliverables for the Horda Platform, with the final aim of refining inputs for the local and basin-scale Numerical Geomechanical Smeaheia Model.

1 Stress drop analysis

1.1 Introduction

In this section we provide an overview on the work within task 2.3. In task 2.3 we proposed to estimate stress drop of the event catalog developed in task 2.1.

Measurement of earthquake stress drop helps to further characterise the geodynamic behaviour of the storage sites. Stress drop, i.e., the difference of the stress magnitude before and after an earthquake can be measured from the spectrum of the earthquake source signature.

We aim to estimate stress drops by applying a data-driven iterative least-squares stacking approach (Shearer et al., 2006), which requires a large dataset with an ideally even event-station distribution to best use the redundancy contained in the data. For this work we decided to focus on the Horda platform area.

We started to expand the original database to include many more small magnitude events since a wide-magnitude range is also required by the method. A lot of time was spent on preparing a complete as possible dataset and adapting existing code routines to work with these data. We also include comprehensive synthetic test scenarios to better evaluate the limitations of the method and data.

We focus on the following points:

- A description on the Horda platform database.
- The performed analysis to compute source displacement spectra.
- The moment magnitude estimation and comparison to local magnitude.
- The stress drop estimation and experienced challenges.

1.2 The Horda database

The Horda database contains 4669 events located around the Horda platform in the time period 2000-2022 (see Fig. 1). Waveform data were downloaded from public FDSN servers. Only data recorded with a minimum sampling rate of 100 Hz were considered, and stations were also selected based on their epicentral distance to the event with the following criteria:

- max. epicentral distance of 600 km for events reported with a magnitude below 2;
- max. epicentral distance of 800 km for events reported with a magnitude between 2 and 3.5;
- all available data (from the North Sea database) without an epicentral distance limit for events reported with a magnitude above 3.5.

Note that several magnitudes could be reported by different agencies for individual events. To maximise the size of the waveform database, we used the maximum reported magnitude for each event, independently of its type.

In total, waveform data for at least one station could be downloaded for 3289 events. From 2000 to 2009, only a few stations recorded the events (in general less than 10) and the number of recording stations increases over time (see Fig. 2).

From 2018 on, waveform data from the Grane offshore field became available. Similarly, data from the Oseberg and Snorre fields became available during 2019 and 2022, respectively. These data were also included whenever possible.

All waveform data have been resampled to 100 Hz and instrument corrections have been applied.

18,713 P-wave and 18,540 S-wave picks were also available from the ISF bulletin for the selected waveform data, to which we added 1,562 and 1,734 manual picks (for P and S, resp.). In addition, theoretical P- and S-wave arrival times were computed using the Fescan velocity model (Mykkeltveit and Ringdal, 1981). In the absence of manual picks, these can be used to cut data windows around the expected phase arrivals. Occasionally, the events seem wrongly located and the expected arrival times do not match the waveform data. These events are discarded from further analysis and relocating them is outside the scope of this work.

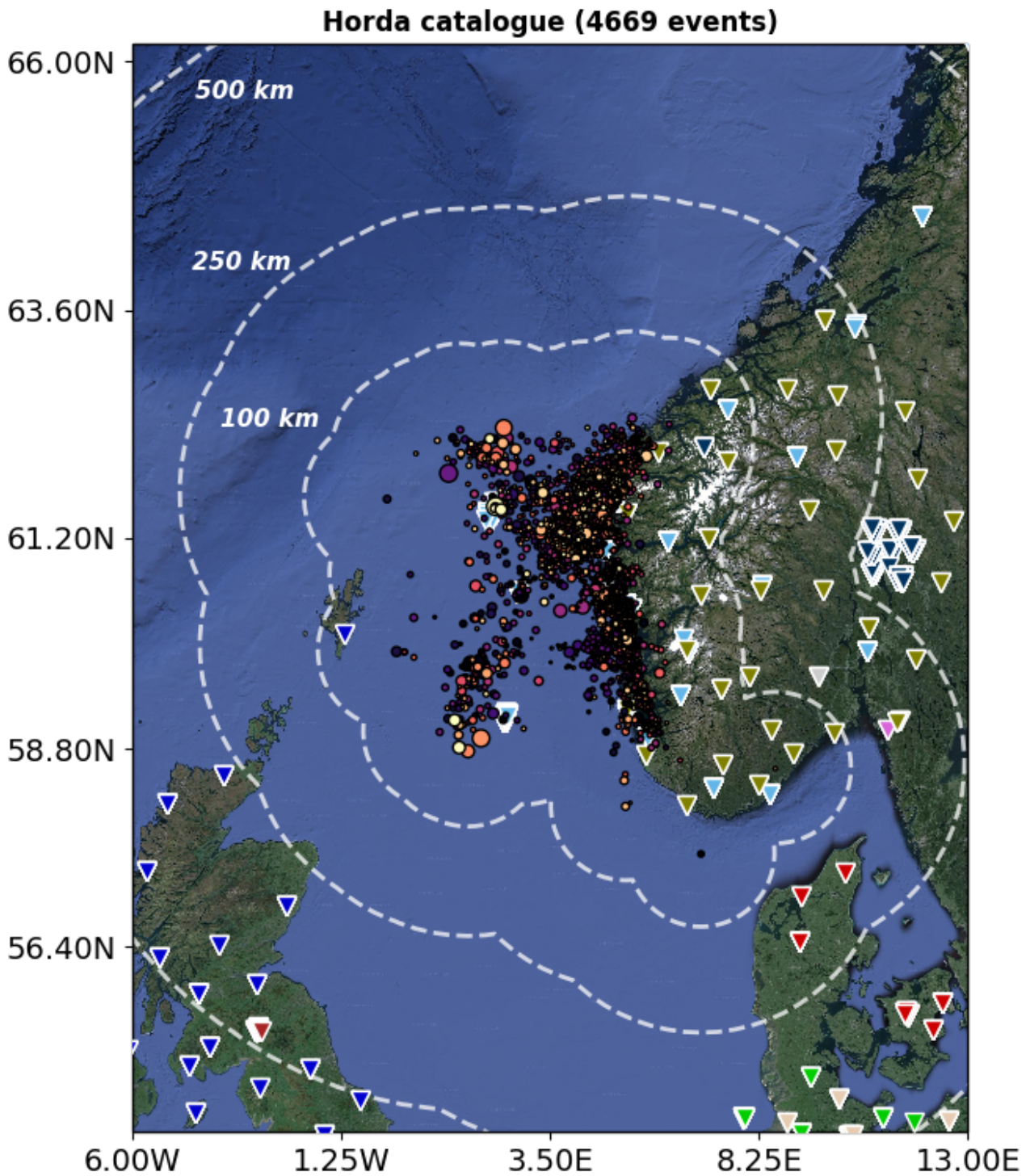


FIGURE 1: Map showing the location of the seismic events around the Horda platform reported by different agencies for the time period 2000-2022. Reversed triangles represent seismic stations coloured by network.

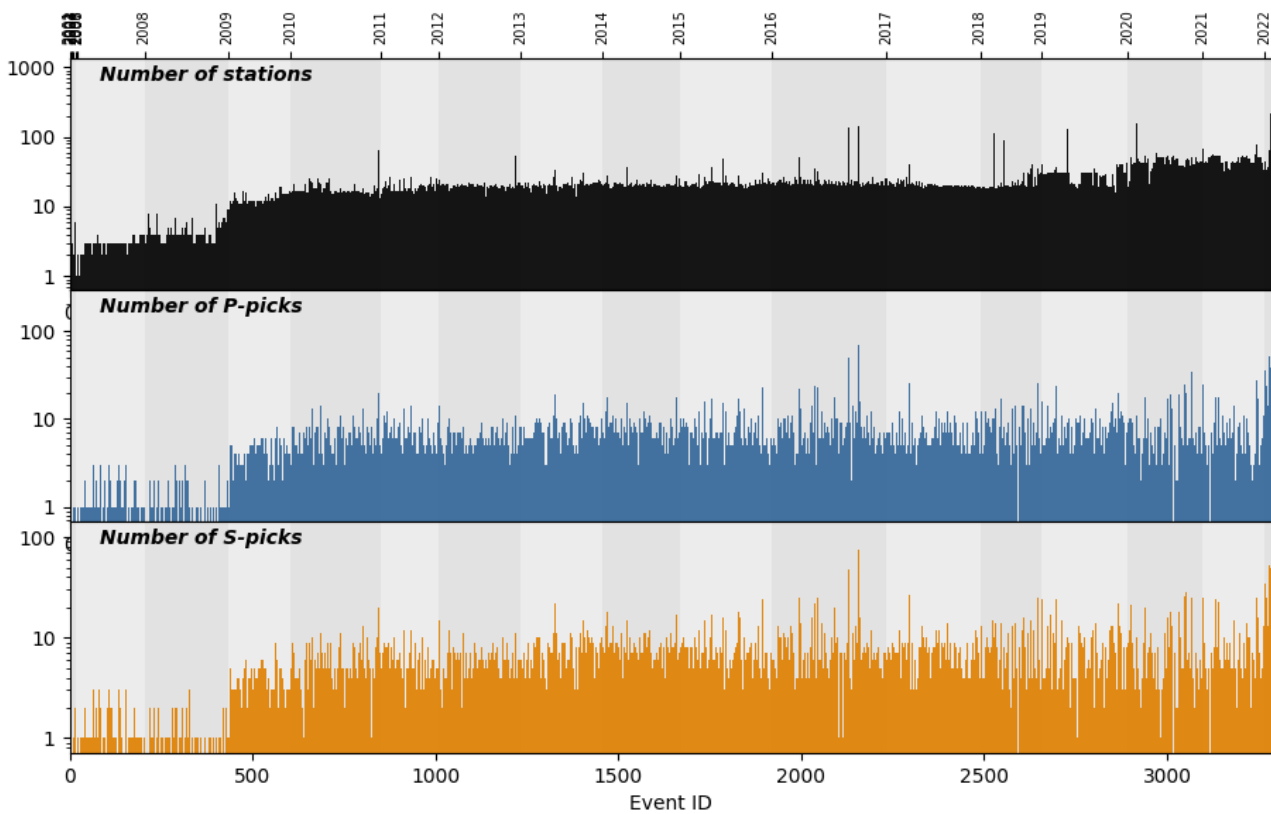


FIGURE 2: Histograms showing the distribution of the number of stations (top), the number of P-wave picks (middle) and the number of S-wave picks (bottom) over time.

1.3 Spectral analysis

1.3.1 Displacement spectra

We compute P-wave and S-wave displacement spectra for the entire Horda waveform database using a multi-taper approach (Prieto et al., 2009). For the spectral estimation we cut 10 sec long time windows starting 0.5 sec before the phase arrival. Manual P-pick and S-pick arrivals are preferred but theoretical phase arrivals may be used if at least one manual pick is available for a given trace. All spectra have been resampled to 100 Hz. We also compute noise spectra from a time window of the same length just before the P-wave arrival.

Two example events are shown in Figure 3 and 4 for M 3.3 and M 1.0. For some traces the chosen 10 sec time window may be too short to cover the entire S-wave coda. However, for longer time windows the S-wave would start to contaminate the P-wave window for more traces. Note that especially for smaller events the signal to noise ratio (SNR) will be poor below frequencies around 2-3 Hz.

In summary, P-wave and S-wave displacement spectra of 3280 events have been computed. In the following work we focus on the S-wave spectra due to generally higher SNR.

1.3.2 Spectral separation method

We require a minimum signal-to noise ratio (SNR) of at least 3 in the frequency range between 3 Hz and 25 Hz. The SNR is estimated using a 10 sample moving window average over 20 neighbouring frequency sample points with regular sampling in the log domain. The noise window is selected before

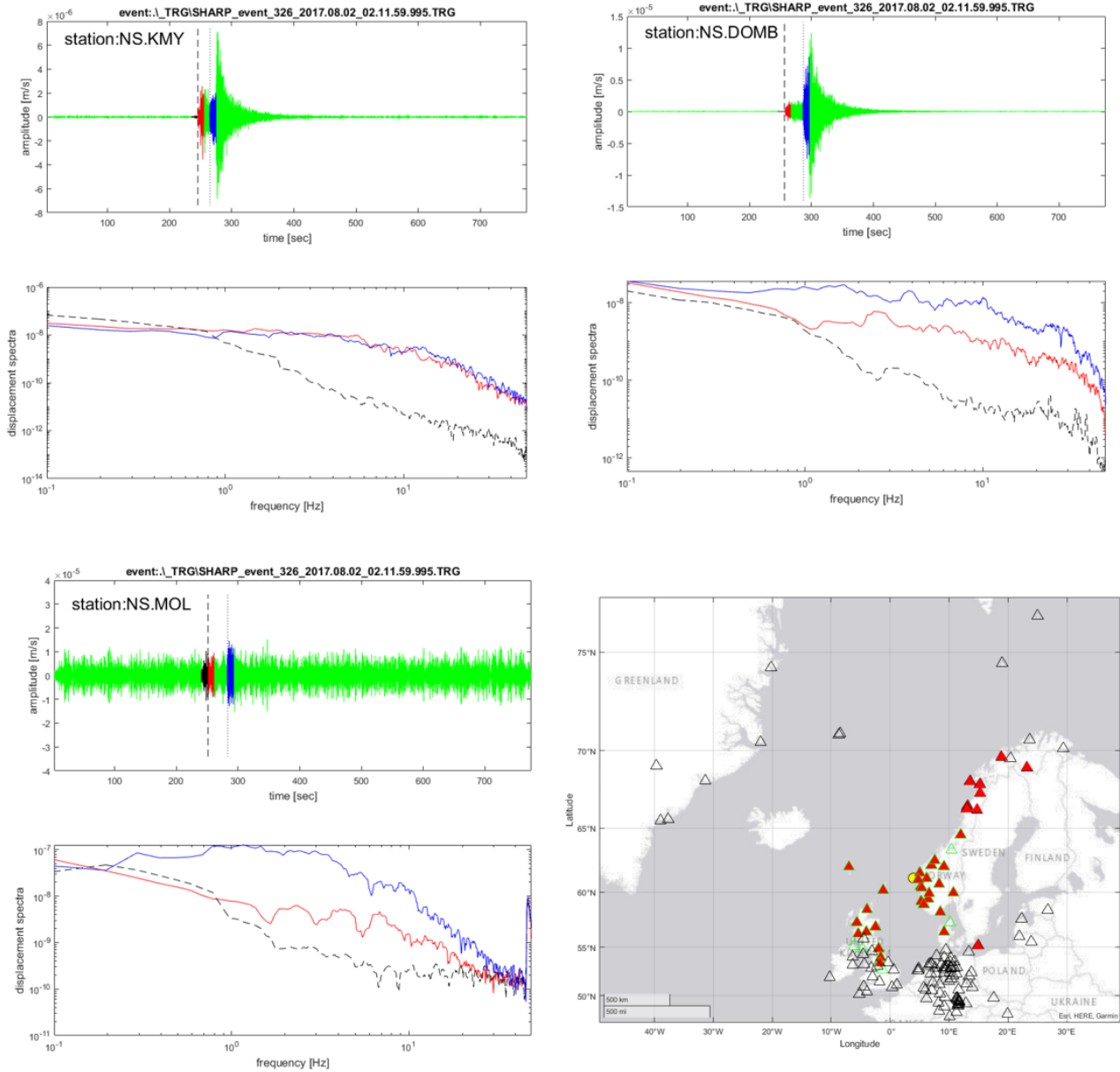


FIGURE 3: Example M_L 3.3 event with waveform (top) and displacement spectra (bottom) for P-wave (red) and S-wave (green) at selected stations. The black dashed line in the spectrum shows the noise level. The map indicated the event location (yellow circle) and all available station data (triangles: red-filled=P-wave picks available; green outlines: S-wave picks available).

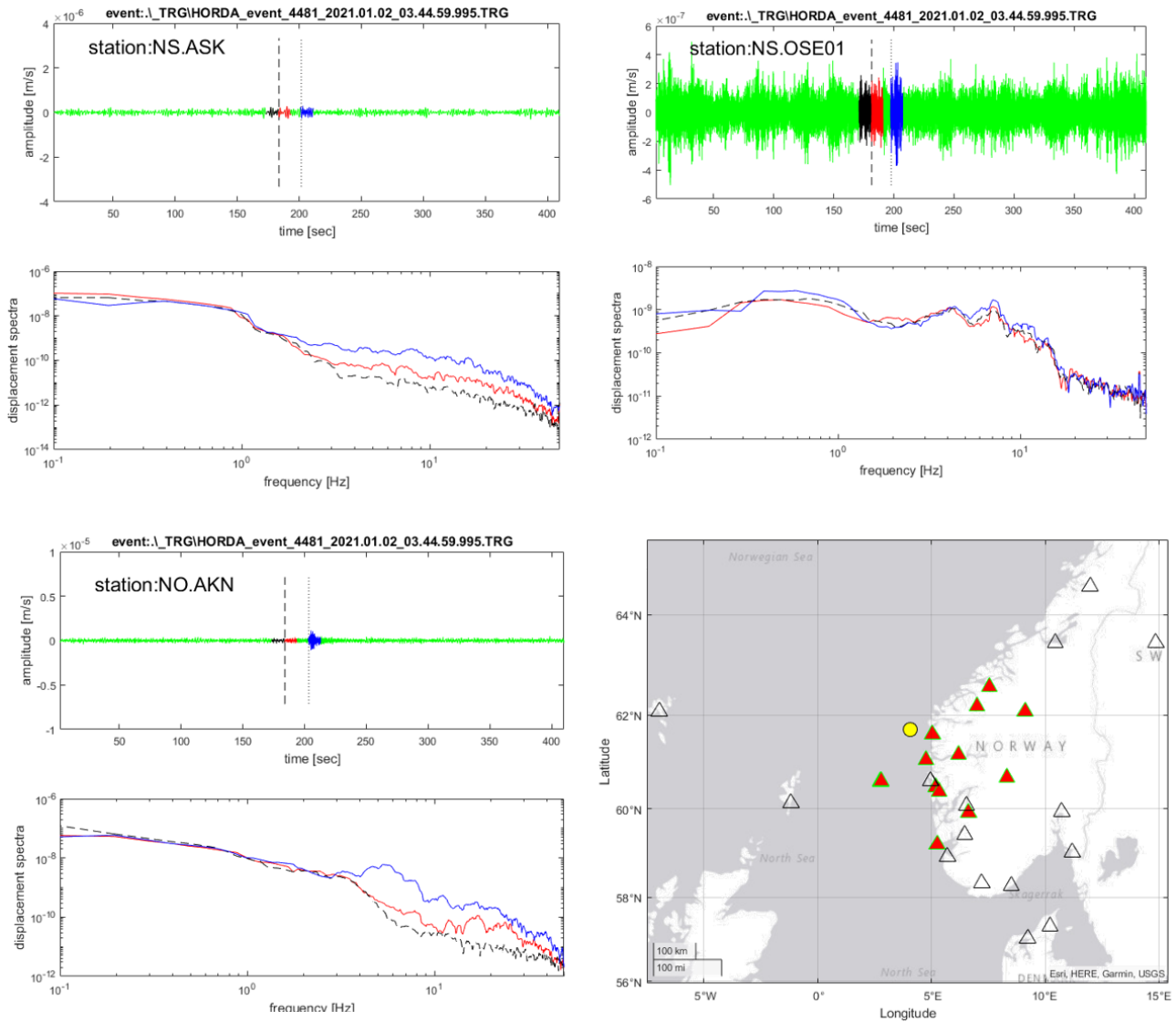


FIGURE 4: Example M_L 1.0 event with waveform (top) and displacement spectra (bottom) for P-wave (red) and S-wave (green) at selected stations. The black dashed line in the spectrum shows the noise level. The map indicated the event location (yellow circle) and all available station data (triangles: red-filled = P-wave picks available; green outlines = S-wave picks available).

the P-wave arrival. We also require each event to be recorded by at least six different traces (i.e., 3 stations) including both, N and E components, in order to average out directivity effects between different azimuths. We furthermore exclude traces with an epicentral distance larger than 350 km. This results in processing of 2894 events including 24,565 traces recorded at 32 different stations.

In the log domain, the displacement spectrum can be described by a linear combination of the source, the attenuation along the travel path, and site effects at the receiver. To study the earthquake source we can separate the source term from other terms by means of an iterative least-squares stacking approach where we exploit the redundancy contained in the data following

$$d_{ij}(f) = e_i(f) + s_j(f) + t_{k(i,j)}(f) + r_{ij},$$

where d_{ij} is the displacement spectra, e_i is the source term, s_j is the station term, $t_{k(i,j)}$ is the travel path term and $r_{i,j}$ is the residual term.

The traveltimes term is discretized in 2 s bins. For further details about the spectral stacking approach, the reader is referred to Shearer et al., 2006 and Allmann and Shearer, 2007. Note that with this method we isolate relative variations of the source spectra between all events and we have to apply an empirical correction with the assumption of a specific source model afterwards to obtain absolute source spectra. This is described further in section 1.5.

Figure 5 shows a map of all crossing paths between stations and events in the dataset. This does not yet exclude traces with poor SNR nor limited by epicentral distances. While we can expect some ray-path crossing for larger magnitude events we also note that especially for the smaller magnitude events the event-station distribution is not ideal. Most of the events in the database are only recorded well at stations located along the Norwegian coast while all events are located offshore to one side. Note that this uneven distribution may result in difficulties in properly separating the different spectral terms.

1.4 Moment magnitude

1.4.1 Method

The determination of the moment magnitude M_w is often not performed on a routine basis. It is a physical source parameter describing the earthquake size and is less dependent on assumptions on attenuation relations compared to the commonly computed local magnitude M_L . It can be difficult to compare M_L estimates from different studies and large differences of up to one order of magnitude are not uncommon. Nevertheless, simple empirical scaling relations between M_L and M_w are commonly used to estimate M_w . For larger magnitude events (≥ 3) a 1:1 scaling between M_L and M_w is often used.

The seismic moment M_0 is proportional to the long-period spectral amplitude Ω_0 of the source spectrum below the corner frequency. We use the spectral model described by Brune, 1970 as

$$u(f) = \frac{\Omega_0}{1 + (f/f_c)^2},$$

where Ω_0 is the long-period spectral amplitude, f_c is the corner frequency.

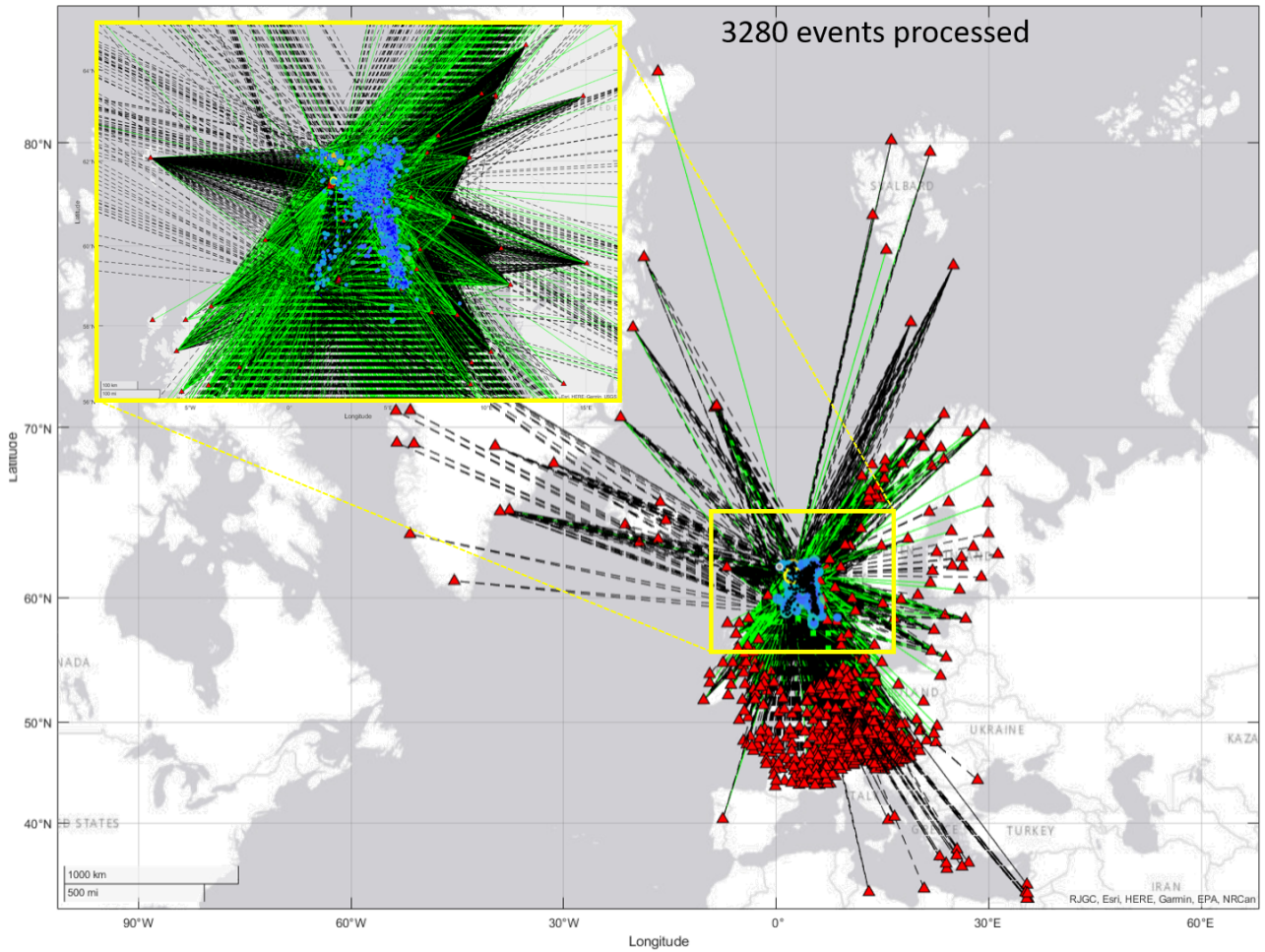


FIGURE 5: Map of the path distribution between all events (blue circles) and stations (red triangles) in the database. Phase picks are only available for event-station pairs shown by a green line.

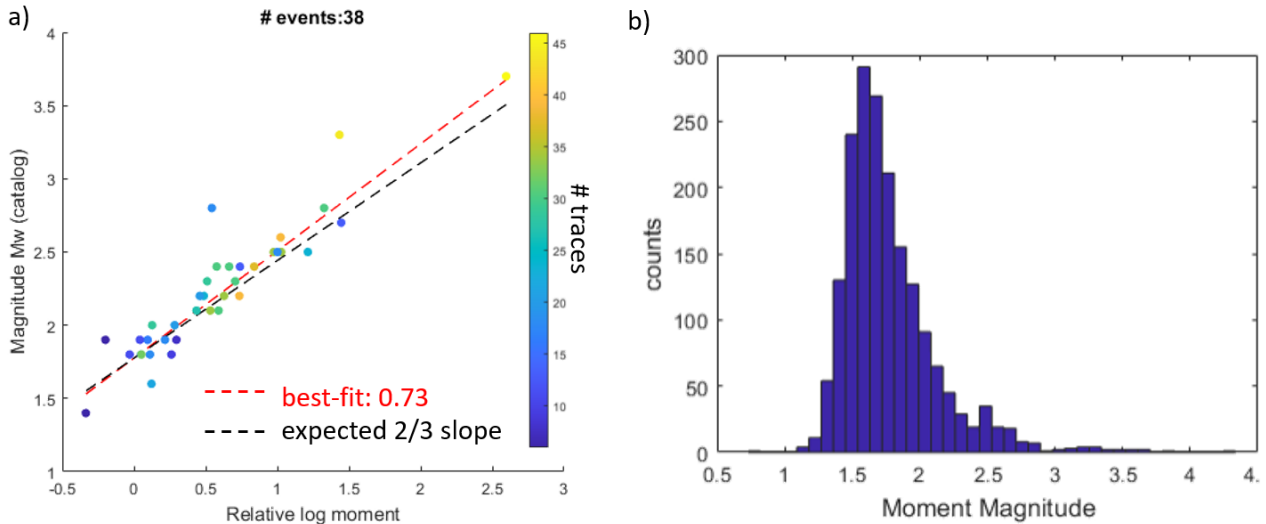


FIGURE 6: a) Moment magnitude M_W estimates from the Horda catalog of 38 events versus relative moment estimates. The black dashed line shows a 2/3 relation and the red dashed line the best linear fit with a slope of 0.73. The color denotes number of traces per event. b) Histogram distribution of M_W estimates of 1853 events.

We estimate the relative seismic moment from the average spectral amplitude between 2 Hz and 4 Hz of each relative source spectrum. We cannot estimate Ω_0 at lower frequencies since the SNR deteriorates rapidly below about 2 Hz, especially for smaller magnitude events. The calibration to absolute M_W can be performed with a small percentage of the data set (38 events) for which independently obtained absolute M_W estimates are available in the catalog. We observe a clear linear correlation between the estimates with a best-fit of $M_W(\text{catalog}) = 0.73 \Omega_O + 1.78$ (Figure 6). This is close to the expected 2/3 slope from the well-know relation (Hanks and Kanamori, 1979):

$$M_W = \frac{2}{3} \log_{10}(M_0) - 10.7$$

1.4.2 Comparison to local magnitude

Furthermore, we compare the estimated M_W to local magnitude M_L from the catalog (Figure 7). We find that a 1:1 relationship does not fit the data. This is consistent with observations from other studies (e.g., Hanks and Boore, 1984; Grünthal et al., 2009; Goertz-Allmann et al., 2011). For regional seismicity in Switzerland a three-step scaling relation was developed by Goertz-Allmann et al., 2011. In general our M_W estimates are in agreement with this relation (see Figure 7 b). The observed large scatter of individual events may result from large uncertainties in the M_L catalog or issues in the spectral estimates. Further analysis of selected events may help to further reduce this scatter.

1.5 Source spectral analysis

In this task we aim to estimate stress drop of individual events from the corner frequency of the source spectra based on a certain source model assumption.

As described in section 1.3, we applied a data-driven method using a spectral stacking approach that exploits the redundancy of the captured wave paths for the separation of source, path. In order to

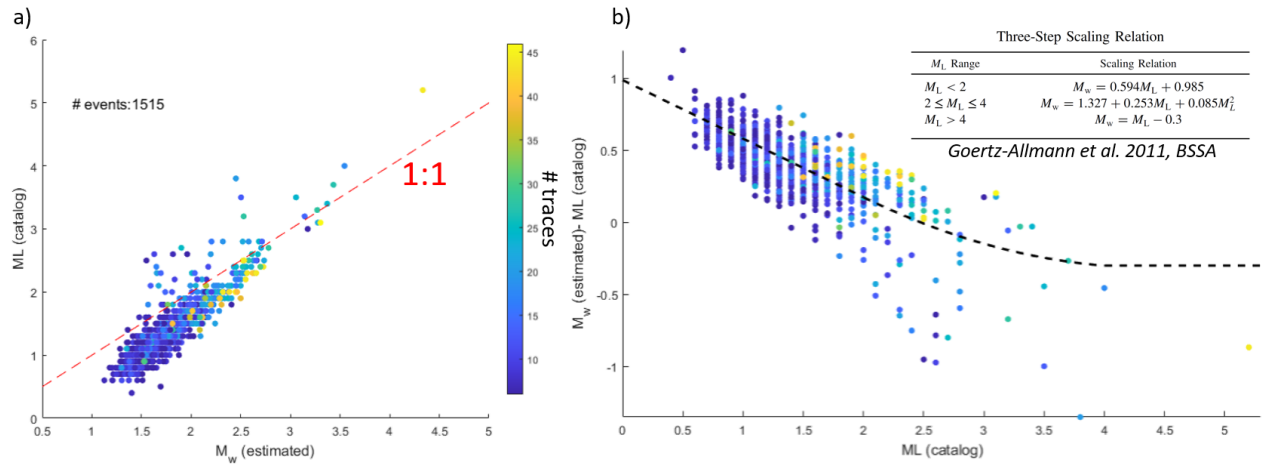


FIGURE 7: a) Catalog M_L versus estimated M_W . The red dashed line shows a 1:1 relationship. b) Difference between catalog M_L and estimated M_W versus catalog M_L . The black dashed line shows the three-step scaling relation developed by Goertz-Allmann et al., 2011 from seismicity in Switzerland. Color denotes number of traces per event.

correct the relative source spectra to absolute spectral shapes, we estimate an empirical correction spectrum (ECS). First, all isolated source spectra are stacked into 0.2 units of M_W (see Figure 8a). Secondly, we simultaneously fit an ω^2 source model (Brune, 1970) with constant stress drop across magnitudes to the spectral stacks (Figure 8 a and b).

The underlying source model assumption is a circular fault where stress drop $\Delta\sigma$ can then be determined, using the seismic moment M_0 and the source radius r , as (Eshelby, 1957)

$$\Delta\sigma = \frac{7}{16} \left(\frac{M_0}{r^3} \right).$$

The source dimension can be related to the corner frequency f_c as

$$f_c = \frac{k\beta}{r}, \quad \Delta\sigma = \frac{7}{16} M_0 \left(\frac{f_c}{k\beta} \right)^3.$$

We only include magnitude bins with a sufficient number of event stacks per bin for the spectral fitting. In this case we include M_W bins between 1.3 and 2.5 with 50+ events per bin. The average difference between the best-fitting model and the observed spectral stacks at each frequency sample results in the empirical correction spectrum (ECS). We observe that a constant parameter model with a fixed stress drop of 3 MPa and a fall-off rate of 2 does not fit the data well (Figure 8 b). The smaller magnitude bins are lacking the higher frequencies compared to a constant self-similar model whereas the higher magnitude bins have higher than expected spectral content. If we allow stress drop to be variable for each magnitude bin the residual is significantly reduced. This suggests that only with a strong dependence of stress drop and magnitudes we are able to improve the apparent fit to the data (Figure 8 c). The lowest magnitude bin results in a best-fitting stress drop of 0.4 MPa and increases systematically to 16 MPa for the highest magnitude bin.

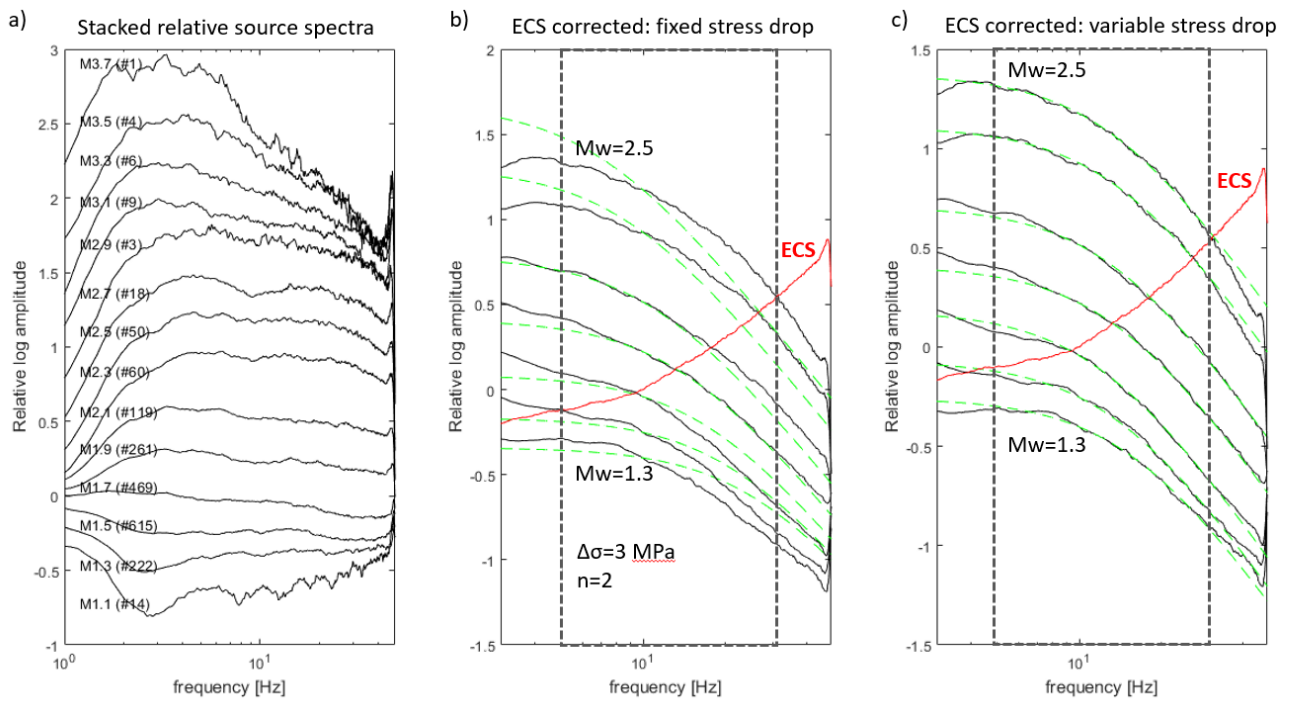


FIGURE 8: a) Relative source spectra stacked in 0.2 moment magnitude bins. The number of events per bin is labeled. b) ECS-corrected source spectral bins (black lines) compared to a constant 3 MPa source model with a fall-off rate of 2 (green dashed lines). c) ECS-corrected source spectral bins (black lines) compared to model with variable stress drop per magnitude bin. The empirical correction spectrum (ECS) is shown by the red line. The black dashed box indicates the used frequency fitting range.

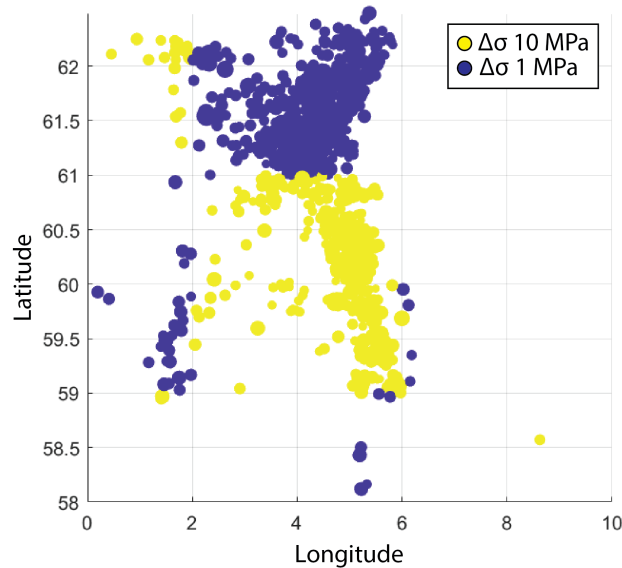


FIGURE 9: Input checker-board event stress drop distribution.

This strongly points to a bias in the inversion and it suggests that the attenuation effects could not be sufficiently removed from the source spectra. We therefore cannot just continue to estimate stress drop of individual events since results will not be reliable. We highly suspect that the uneven data distribution in the Horda database and in the end its limited crossing ray path coverage does not allow for the application of the spectral stacking method.

We further investigated this with a series of synthetic tests.

1.6 Synthetic tests

We carry out a series of synthetic tests to evaluate the performance of the spectral stacking method for stress drop estimation of the Horda database. Here we compare inversion results of regularly spaced receiver grids and different receiver combinations based on the real-data station distribution. For each synthetic test scenario the source locations and event magnitudes are based on the real-data from the Horda database. We assign an input stress drop for each event of 1 MPa or 10 MPa in a checker-board fashion with 4 degree and 2 degree binning in longitude and latitude, respectively (see Figure 9).

The synthetic displacement spectra are computed by combining individual source, site, and travelpath contributions (Figure 10). The source spectra are based on the Ω^2 -source model with a fixed falloff rate of 2 and a constant S-wave velocity of 3500 m/s. The site spectra are randomly created from various mathematical functions. The travelpath spectra $t_{k(i,j)}$ are computed from the traveltime for each source-receiver pair and a constant frequency independent quality factor Q following

$$t^* = tt_{k(i,j)}/Q; \quad slope = -1.364 t^*; \quad t_{k(i,j)} = slope f.$$

We use input Q of 150 or 1000 for different scenarios. A small random residual spectrum is also added to each combined displacement spectrum.

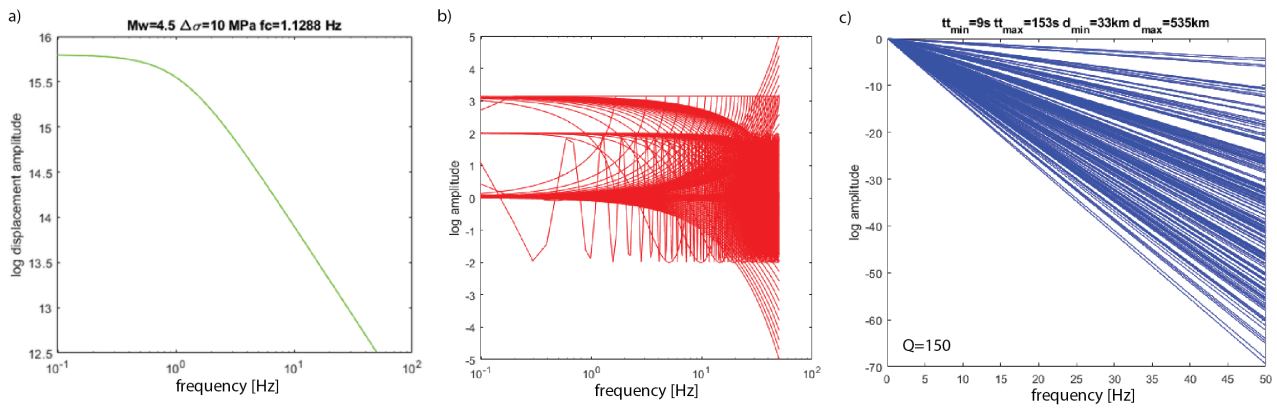


FIGURE 10: Example of input a) source, b) receiver, and c) travelttime spectra.

1.6.1 Synthetic case I: regular station grid

In the first synthetic example we place 169 regularly distributed stations around the area of interest (Figure 11). Using the real-data event distribution we end up with over 555,000 traces. Two synthetic scenarios were computed for this set-up using input Q of 150 and 1000, respectively. For both scenarios, inversion results are stable and input source parameters are overall well recovered (Figure 12). A constant parameter source model with a stress drop of 1.5 MPa fits the data well and individual source spectral fits can be well estimated. Figure 13 shows that magnitudes are almost perfectly recovered below $M < 2.5$. As for the real data, magnitudes are estimated from the low-frequency plateau level between 1 Hz and 3 Hz. Magnitude estimates for larger events are clearly underestimated as a result of this limited bandwidth. Figure 14 and 15 summarise inverted stress drop estimates of input data using Q of 150 and 1000, respectively. In both cases the overall spatial stress drop pattern is recovered. However, quite some scatter in absolute stress drop values is observed in the data. Especially the higher stress drop values (10 MPa) of small magnitude events can be underestimated by over one order of magnitude. Similarly, we significantly underestimate the lower stress drop values of large magnitude events. Again this is driven by the limited fitting bandwidth. Corner frequencies are estimated by fitting spectra between 1-30 Hz, which is directed by the signal-to-noise levels for the real data. The underestimation is even stronger for the $Q=150$ case. This also suggests that we still can not entirely separate source and path effects in this synthetic case.

1.6.2 Synthetic case II: real-station distribution

In the following we present several synthetic data scenarios based on real-station and event distributions (see Figure 16). The different scenarios include:

- S2.1 Onshore stations within 350 km distance to sources are used (38 stations total). In addition, only real-data event-station pair distributions are included. In the real data many events are only recorded well with clear P-wave and/or S-wave picks at few receivers. Also the number of recordings change over time with more stations available in more recent times. This results in a total of 55,960 traces.
- S2.2 Onshore stations within 350 km distance to the sources are used (38 stations total). We include all possible event-station pairs. This results in a total of 88,372 traces.

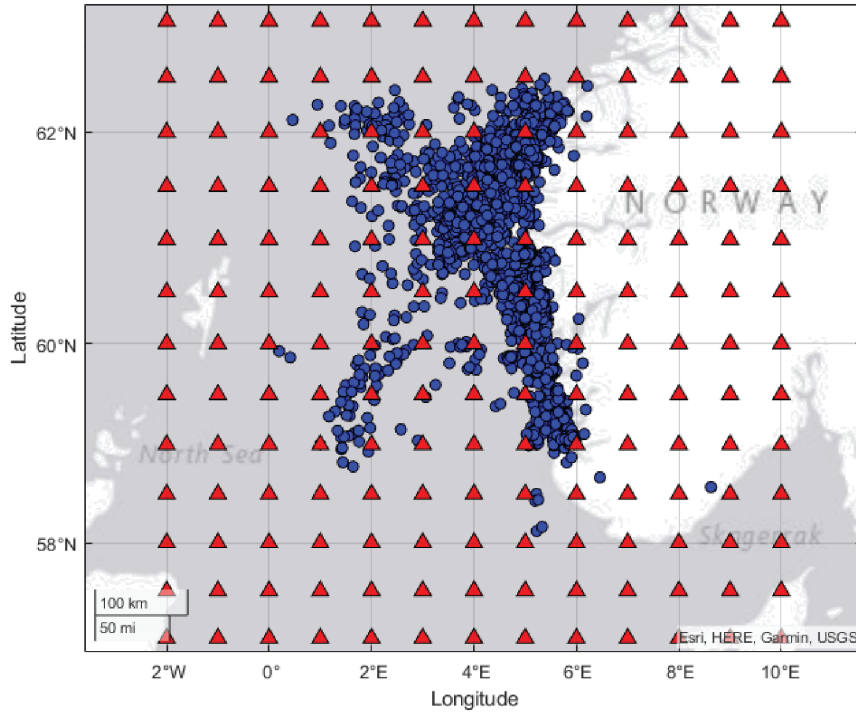


FIGURE 11: Synthetic test geometry with 169 regularly spaced sensors (red triangles) with 1 degree bins in longitude and 0.5 degree bins in latitude. Event locations are used from the real data distribution (blue circles).

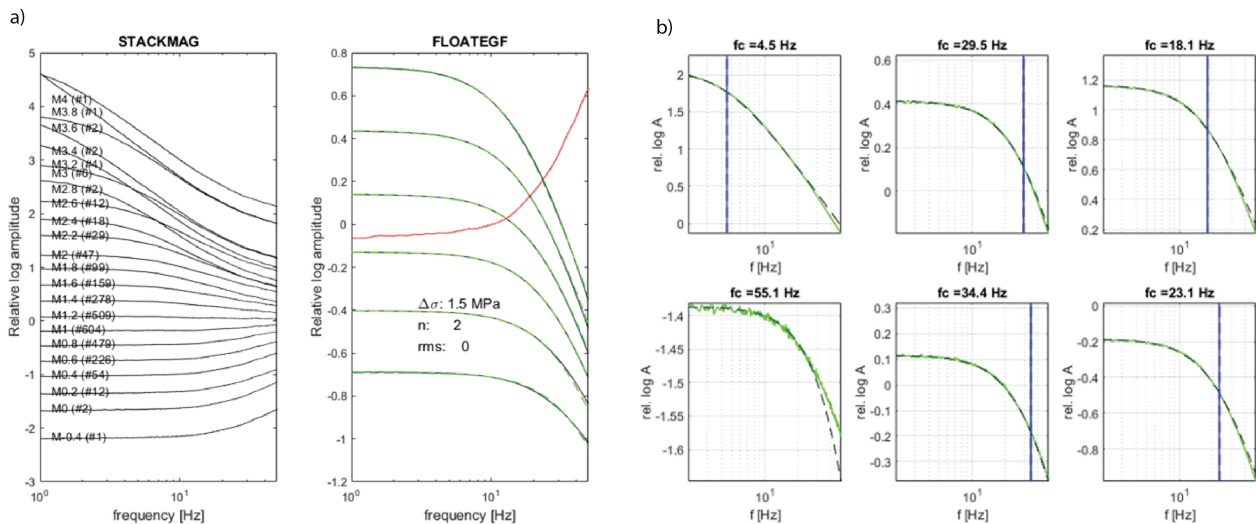


FIGURE 12: a) Synthetic results of relative source spectra stacked in 0.2 moment magnitude bins. The number of events per bin is labelled. The empirical correction spectrum ECS is shown in red. ECS-corrected source spectral bins (black lines) compared to a constant best-fitting source model with a stress drop of 1.5 MPa and a fall-off rate n of 2 (green dashed lines). b) Source spectra of six example events (green lines) together with the best-fitting model (black dashed). The vertical blue line shows the event corner frequency f_c .

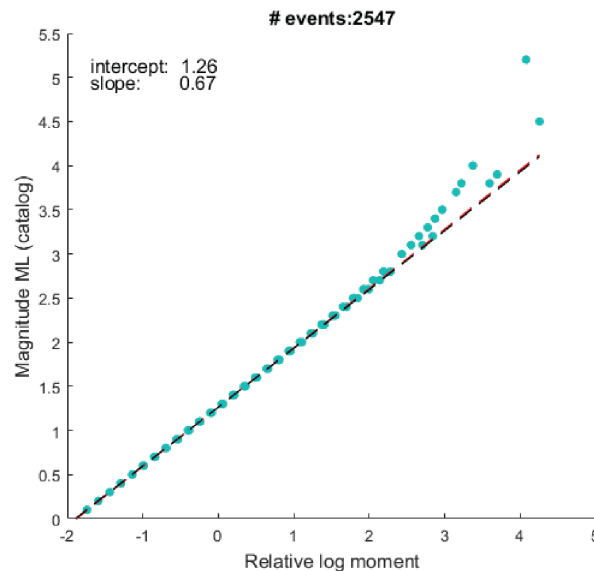


FIGURE 13: Catalog magnitude (input) versus relative moment estimates for synthetic test 1. The dashed line shows the best linear fit with a slope of 0.69.

S2.3 Onshore and selected offshore stations within 350 km distance to the sources are used (68 stations total). We include all possible event-station pairs. This results in a total of 185,726 traces.

S2.4 Onshore and selected offshore stations within 1000 km distance to the sources are used (521 stations total). We include all possible event-station pairs. This results in a total of 1,093,481 traces.

In general, magnitudes can be recovered for all scenarios (Figure 17). For all cases we observe a bias of the larger magnitudes above three due to saturation effects from the fixed frequency range (1 Hz and 3 Hz) used for spectral plateau estimation. It is interesting to note that we observe the smallest scatter in case S2.3 and we see slightly larger scatter if stations at larger distances are included (S2.4). The overall observed scatter in magnitude estimation is largest in case S2.1 with only limited source-receiver pairs included. Furthermore, higher attenuation (lower Q-values) in the input data can lead to strong bias in magnitude estimation if the inversion can not properly remove path effects from the data. This bias is especially seen for case S2.1 resulting from a very unstable spectral inversion (Figure 18 a). In all other cases a good fit between the data and the theoretical model is obtained (Figure 18 b). This becomes also evident in the final stress drop estimates where case S2.1 cannot recover any input values (Figure 19 and 20). The general input checker-board stress drop pattern can be recovered for all other cases S2.2 to S2.4 but with different levels of scatter and bias. Again the best result is obtained for case S2.3. It is interesting to note that the scatter in S2.3 is even smaller compared to the synthetic case I with a regular station grid (Figure 15).

From the conducted synthetic tests we learn that the given source-receiver pair distribution of the Horda platform is too limited to properly invert for source spectra and stress drops (S2.1). However, we can show that the overall source-receiver geometry is not hindering a successful inversion of source parameters. A successful inversion requires a larger number of source-receiver pairs (i.e.,

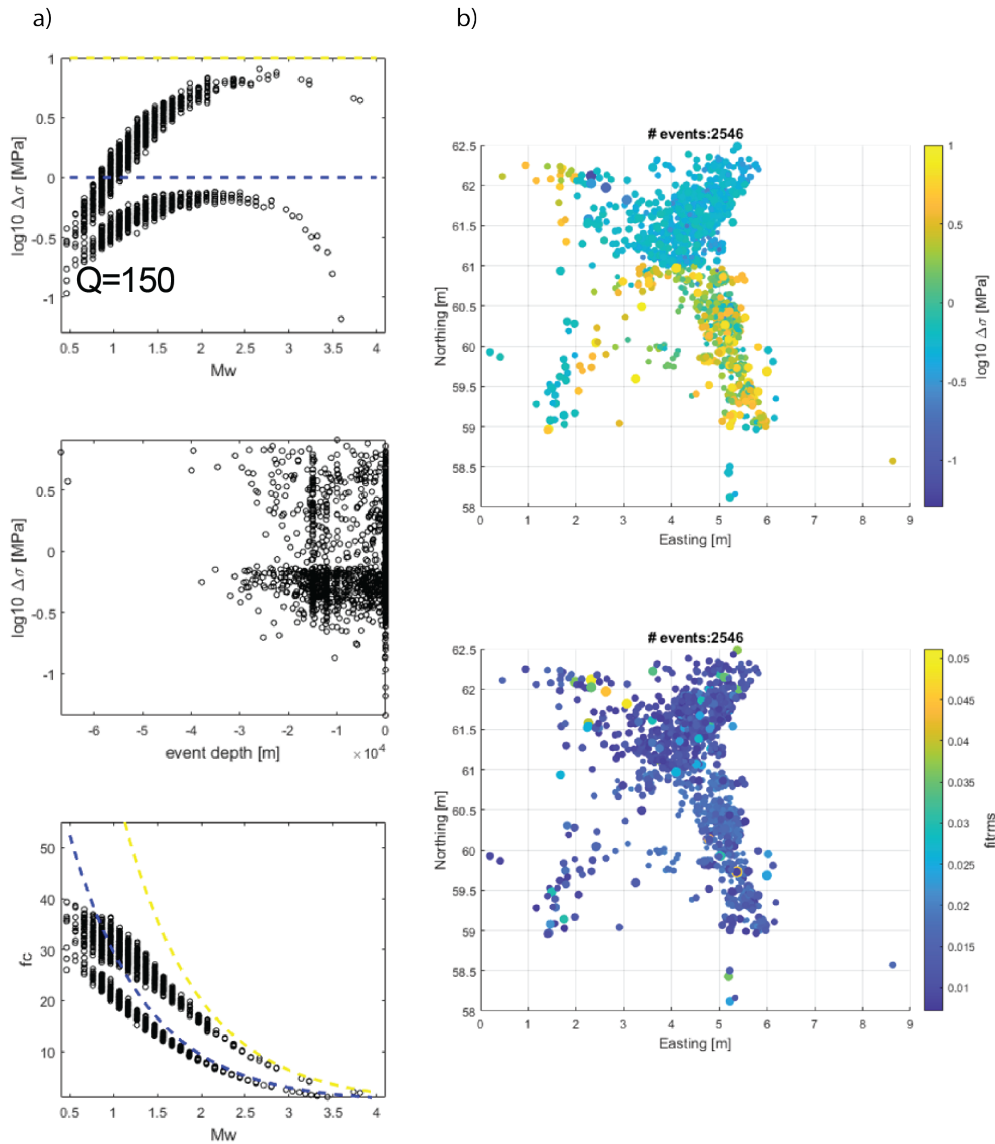


FIGURE 14: Results of inverted stress drop estimates for synthetic test 1 using an input Q-value of 150. a) Comparison of stress drop estimates versus moment magnitude (top) and event depth (middle), and corner frequency versus moment magnitude (bottom). Yellow and blue dashed lines show the input values for 10 MPa and 1 MPa, respectively. b) Spatial stress drop distribution (top) and root mean square residuals (bottom).

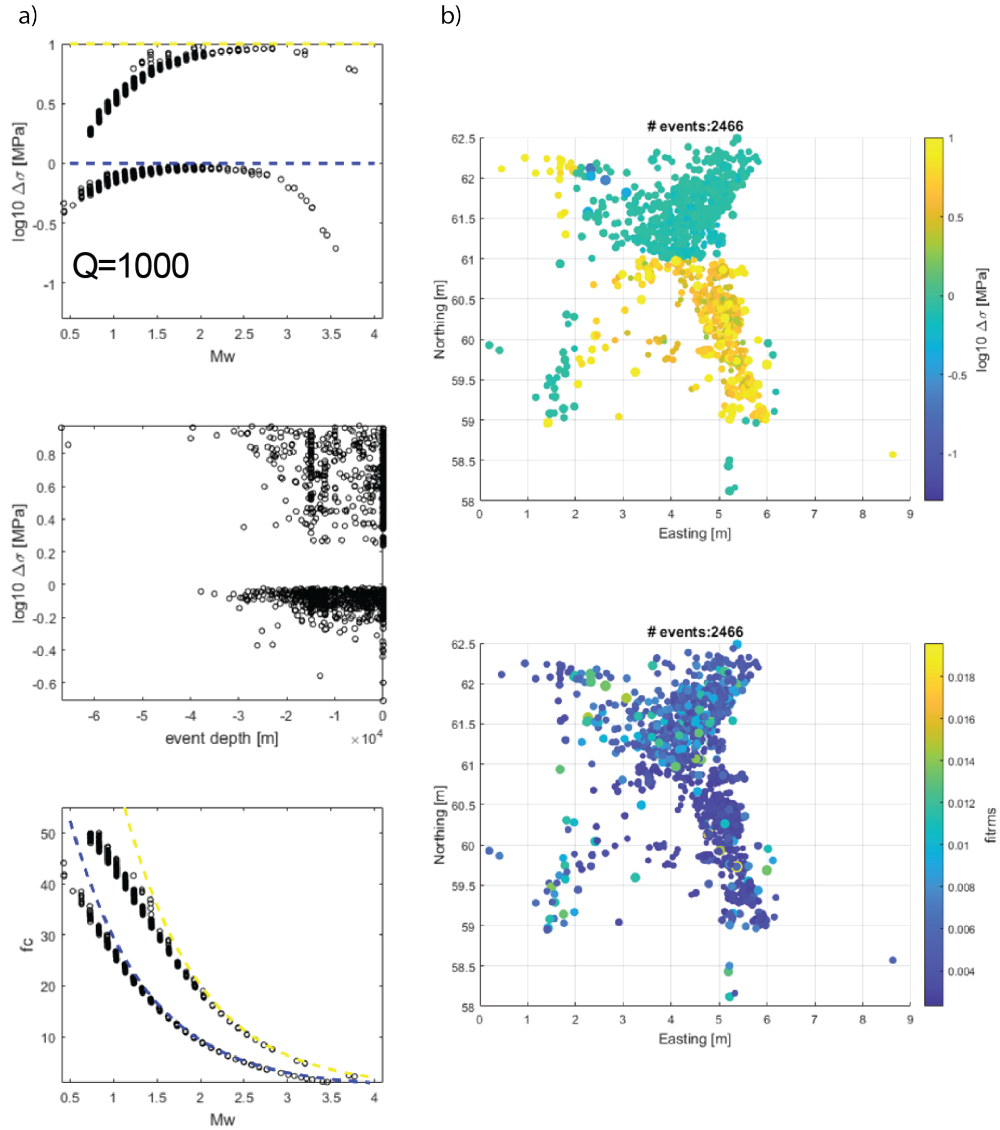


FIGURE 15: Results of inverted stress drop estimates for synthetic test 1 using an input Q-value of 1000. a) Comparison of stress drop estimates versus moment magnitude (top) and event depth (middle), and corner frequency versus moment magnitude (bottom). Yellow and blue dashed lines show the input values for 10 MPa and 1 MPa, respectively. b) Spatial stress drop distribution (top) and root mean square residuals (bottom).

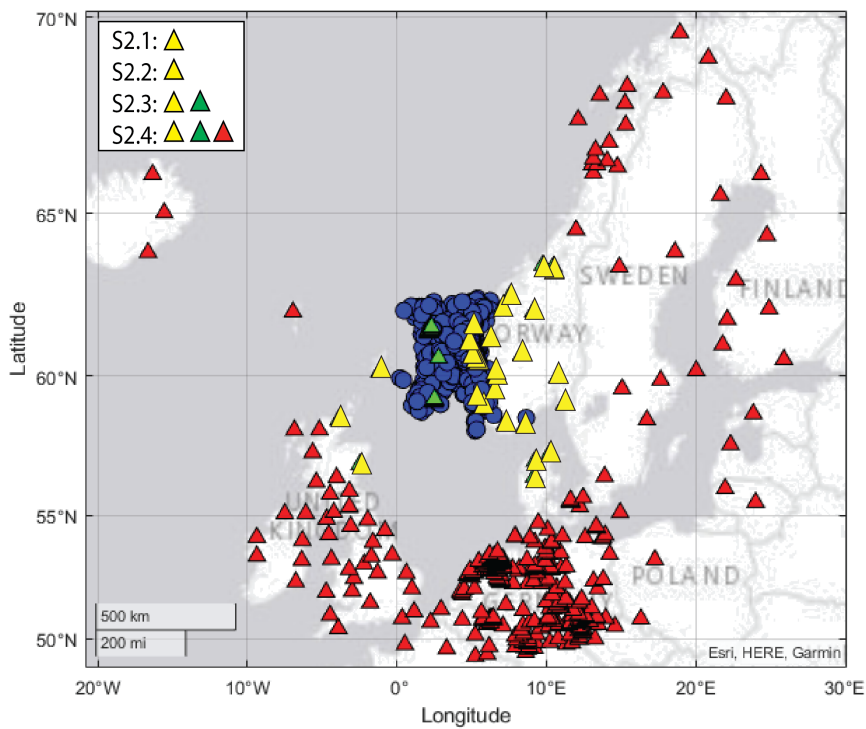


FIGURE 16: Synthetic test geometry with real station distributions. Yellow triangles show all onshore sensors within 350 km to the sources (used in S2.1 and S2.2). Green triangles show additional selected offshore sensors (used in S2.3 and S2.4). Red triangles show all available stations at larger distances up to 1000 km to the sources (used in S2.4). Source locations are based on the real data event distribution (blue circles).

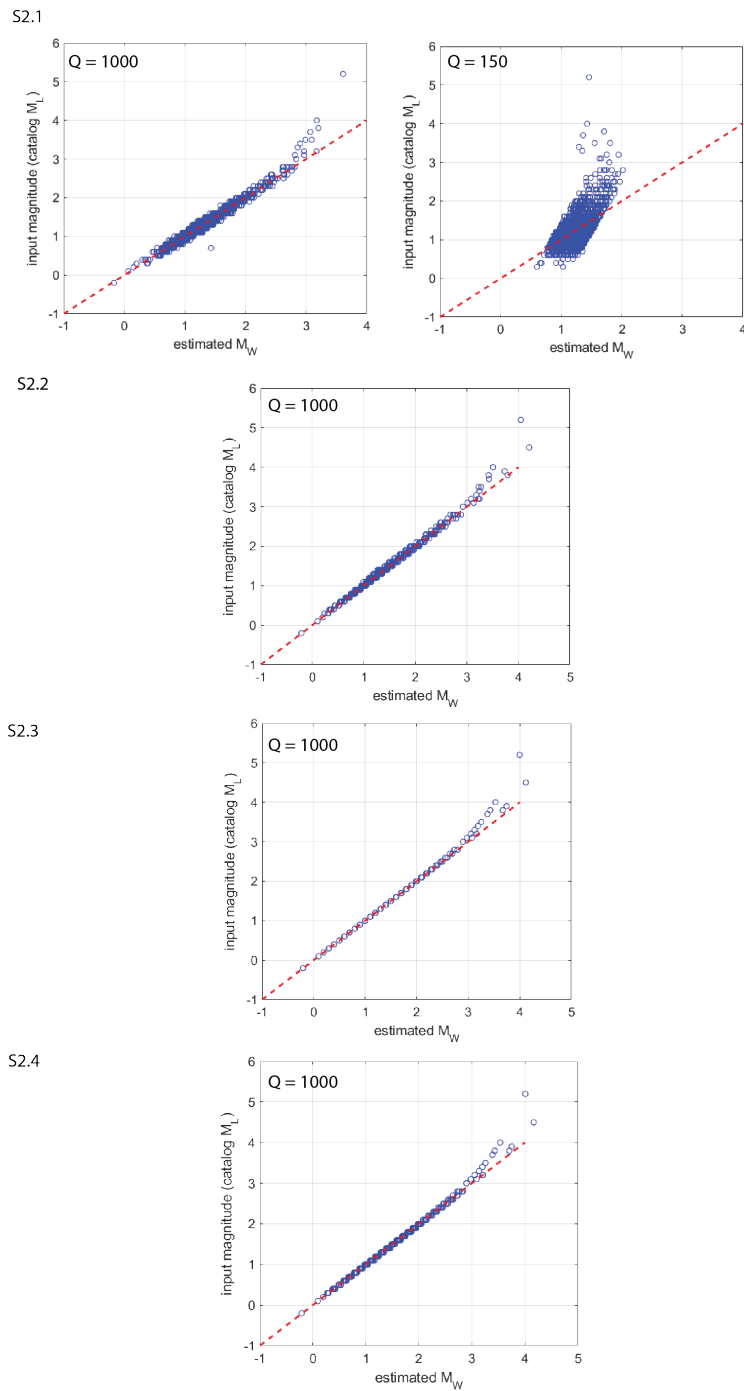


FIGURE 17: Input catalog magnitude (M_L) versus estimated moment magnitude (M_W) for synthetic test S2.1 to S2.4. Input Q values are listed. The dashed red line shows a one to one relation.

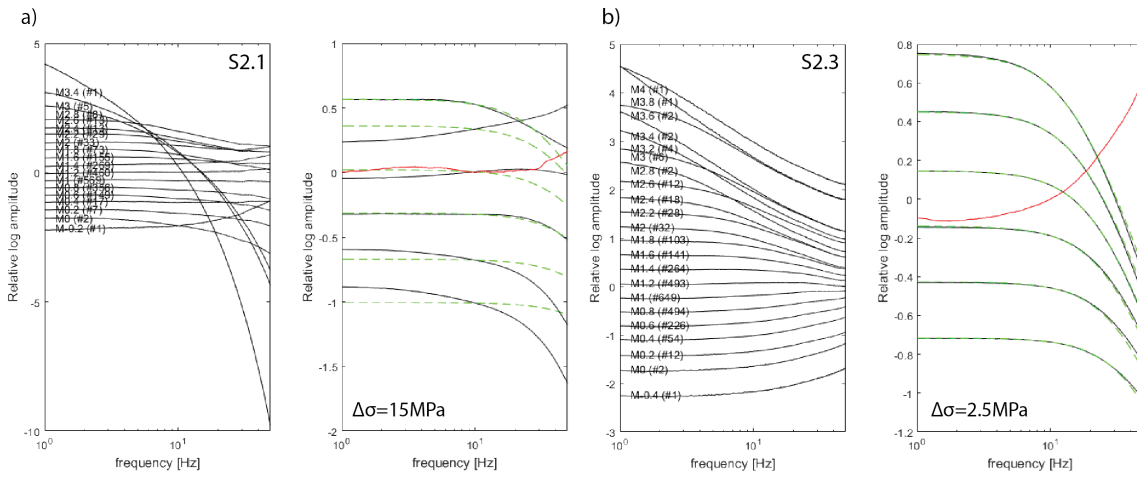


FIGURE 18: Synthetic results of relative source spectra stacked in 0.2 moment magnitude bins. The number of events per bin is labelled. The empirical correction spectrum ECS is shown in red. ECS-corrected source spectral bins (black lines) compared to a constant best-fitting source model with a constant stress drop (green dashed lines). a) Case S2.1 and b) case S2.3.

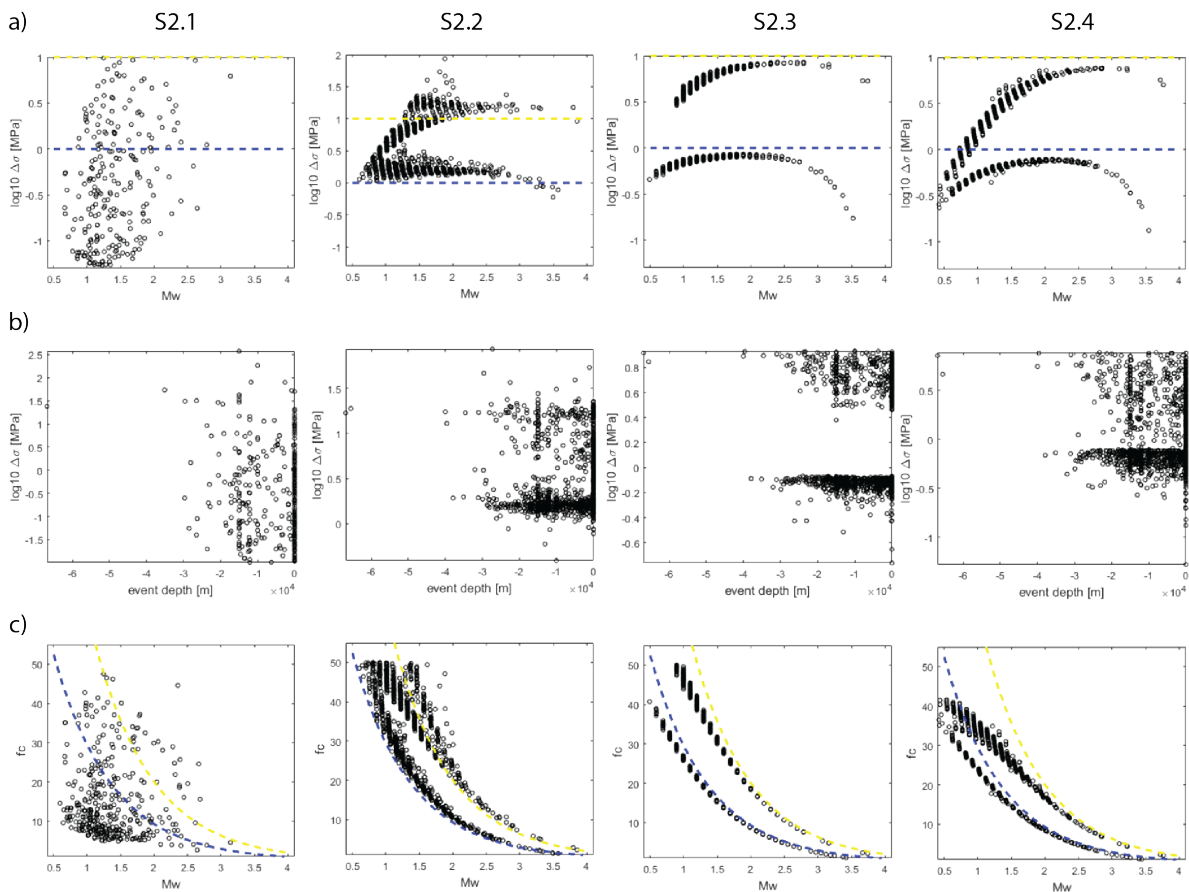


FIGURE 19: Results of inverted stress drop estimates for synthetic tests S2.1 to S2.4 using an input Q-value of 1000. Comparison of a) stress drop estimates versus moment magnitude, b) stress drop estimates versus event depth, and c) corner frequency versus moment magnitude. Yellow and blue dashed lines show the input values for 10 MPa and 1 MPa, respectively.

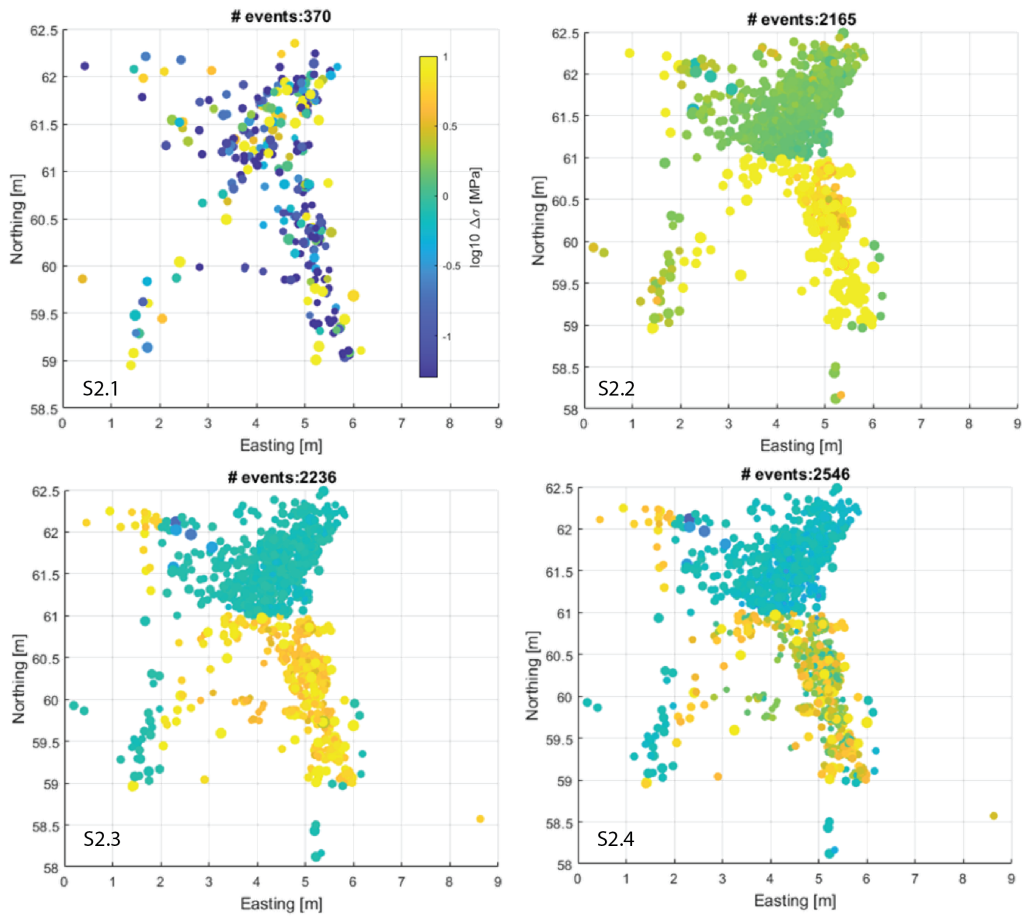


FIGURE 20: Spatial distribution of inverted stress drop estimates for synthetic tests S2.1 to S2.4 using an input Q-value of 1000.

if we assume that each event is recorded by all receivers, S2.2 to S2.4) with more crossing ray path and including a larger range of traveltimes.

1.7 Conclusion of Horda stress drop estimation

The aim of this study was to estimate stress drop of the Horda platform database using a spectral stacking approach. We find that the spectral inversion for separating source contributions from site effects and path effects is unstable for the given event-receiver pair distribution. We therefore conclude that the stress drop estimates are not reliable.

A series of synthetic tests was conducted and the results show that in general it should be possible to apply the spectral stacking method to the given station geometry but a larger number of crossing ray paths with a larger available range of traveltimes is required. This shows that lowering the event detection threshold (i.e., recording smaller magnitude events) by installing denser networks closely distributed around the area of interest will be necessary to apply such methods in the future. We find that stations placed within as well as outside the event cloud can help to further reduce scatter in source parameter estimation. Furthermore, our results also highlight the importance of a sufficient spectral bandwidth to reduce bias in moment magnitude estimations and corner frequencies.

2 Stress data integration

2.1 Introduction

This section focused on the synthesis and integration of stress data for the Horda Platform, aiming to provide constraints for the **Numerical Geomechanical Smeaheia Model** (D1.5: "Calibration and Sharpened Modelling"). The model is divided into two parts: the local- and the basin-scale models. Shallow stresses, constrained by borehole measurements, can help refine the local-scale model. In contrast, deep crust stress data, derived from various seismological methods such as focal mechanisms, stress drop analysis, and stress orientation from the shear-wave splitting method, can inform the basin-scale model. However, stress drop analysis has proven unable to remove the path effect from the spectra due to where most events are located offshore and most stations are located on-shore along the Norwegian coast on one side (see Section 1). Therefore, stress drop results cannot be used in this stress integration.

Shear-wave splitting was possible for the Snorre Field and 24 good quality shear-wave splitting measurements were made out of five earthquakes (details in D2.3). Results indicate a general E-W trend however there is currently insufficient data to interpret σ_H orientation from the shear-wave splitting with confidence.

Furthermore, **Probabilistic Fault Stability Assessment** was conducted and reported in D5.4: "Workflow for reliability assessment". Among the 13 input parameters, initial stress condition include (i) the ratio of horizontal effective stress to vertical effective stress (K_0), (ii) the azimuth of maximum horizontal stress σ_H (expressed as mean and standard deviation) and (iii) the ratio of the maximum horizontal stress to the minimum horizontal stress (σ_{hAR}). Therefore, in the following we will compare stress orientations with the mean and standard deviation values for the azimuth σ_H (ii) reported in D5.4.

2.2 In situ stress orientation for the Horda Platform

Stress magnitudes and stress orientations for the Horda Platform area have been documented in Thompson et al., 2022. Trends of minimum horizontal stresses (σ_h) from the Horda-Tampen area include 46 XLOTs at casing shoes, 8 XLOTs performed at intermediate depths as formation barrier tests (through perforations) and 11 minifrac results (from reservoir sandstones). The general in-situ stress regime in the shallower sediments (**less than 3000 m**) can be characterised as **normal-faulting/extensional** ($\sigma_V > \sigma_H > \sigma_h$, to **horizontally isotropic**, two principal horizontal stress are equal in magnitudes, $\sigma_H = \sigma_h$). Local stress perturbations in close proximity to faults cannot be ruled out, however, the major principal stress is vertical. A degree of horizontal stress anisotropy exists, constrained to lie between $1.01 \leq \sigma_H/\sigma_h \leq 1.27$. It is suggested to consider even the most extreme value in the presence of a normal-faulting stress state.

In situ stress orientation for the Horda Platform in this synthesis consist of:

- the **existing WSM2016 data** (Heidbach et al., 2016b) which include earthquake focal mechanisms data (FMS), borehole data (BO) drilling-induced tensile fractures (DIF) and overcoring (OC);
- the **additional borehole stress observations** reported in D2.2 ([SHARP_report_D2_2.pdf](#)): "Bore-

hole Stress Observations";

- the **updated focal mechanisms catalogue** presented in D2.4 (SHARP_report_D2_4.pdf): "Updated catalog and focal mechanism database" and the **additional moment tensor solutions** computed using a probabilistic approach for the moment tensor estimation (preliminary results are presented in D2.4).

2.2.1 Existing WSM2016 in-situ stress data

Depending on the type of data (FMS, DIF, BO or OC), the WSM2016 includes principal stress azimuths (S1AZ, S2AZ and S3AZ) and plunge (S1PL, S2PL and S3PL), and/or the azimuth of the maximum horizontal stress σ_H (AZI). The quality ranking reported in the WSM2016 (Heidbach et al., 2016a) is defined depending on the data type. For FMS, quality ranking is defined as follows:

- A- and B-qualities: not define for FMS (single focal mechanisms);
- C-quality: Well constraint single event solution ($M \geq 2.5$) (e.g., Centroid Moment Tensor solutions);
- D-quality: Well constrained single event solution ($M < 2.5$);
- E-quality: Mechanism with P-, B-, T-axes all plunging 25° - 40° ; Mechanism with P- and T-axes both plunging 40° - 50° .

M is the event Magnitude and P-, B- and T-axes are the focal mechanism pressure, null and tension, respectively.

For BO from caliper logs, quality ranking is defined as follows:

- A-quality: Wells that have ten or more distinct breakout zones with a combined length >300 m; and with standard deviation (s.d.) $\leq 12^\circ$;
- B-quality: Wells that have at least six distinct breakout zones with a combined length >100 m; and with s.d. $\leq 20^\circ$;
- C-quality: Wells that have at least four distinct breakouts zones with a combined length >30 m; and with s.d. $\leq 25^\circ$;
- D-quality: Wells that have less than four breakouts zones or a combined length <30 m or with s.d. $\leq 25^\circ$;
- E-quality: Wells with no reliable breakouts detected or with extreme scatter of breakout orientations (s.d. $>40^\circ$).

For BOs and DIFs from image logs, quality ranking is defined as follows:

- A-quality: ≥ 10 distinct BO or DIF zones and combined length ≥ 100 m in a single well with s.d. $\leq 12^\circ$;
- B-quality: ≥ 6 distinct BO or DIF zones and combined length ≥ 40 m in a single well with s.d. $\leq 20^\circ$;
- C-quality: ≥ 6 distinct BO or DIF zones and combined length ≥ 20 m in a single well with s.d. $\leq 25^\circ$;

- D-quality: ≥ 4 distinct BO or DIF zones or < 20 m combined length with s.d. $\leq 40^\circ$;
- E-quality: Wells without reliable BO or DIF or with s.d. $> 40^\circ$.

For OC, quality ranking is defined as follows:

- A-quality ≥ 11 measurements with depth ≥ 300 m and s.d. $\leq 12^\circ$;
- B-quality: ≥ 8 measurements with depth ≥ 100 m and s.d. $\leq 20^\circ$;
- C-quality: ≥ 5 measurements with depth ≥ 30 m and s.d. $\leq 25^\circ$;
- D-Quality: ≥ 2 measurements with depth ≥ 10 m and s.d. $\leq 40^\circ$;
- E-quality: < 2 measurements or depth < 10 m or s.d. $> 40^\circ$; Measurements in boreholes extending less than two excavation radii from the excavation wall; Distance to topographic features less than three times the height of the topographic feature.

2.2.2 Additional borehole stress observation

The new borehole stress observation reported in D2.2 include the azimuth of the maximum and minimum horizontal stress σ_H (\equiv AZI in the WSM2016) and σ_h , respectively. These observations consist of 15 new borehole data: 4 new analyses of UK wells just west of the Horda Platform provided by BGS, and 11 new observations provided by Equinor (Fig. 21). The focus region was limited between latitude 60° and 61° , and data indicate a general E-W σ_H off Norway and around the Horda Platform (see Fig. 21 and D2.2 for details). Out of the 11 observation provided by Equinor, which include DIF as well as borehole breakout (BO) observations. Six of them have information on bottom and top failure depth, otherwise only top and bottom borehole depths are included. Furthermore, a quality ranking (from A to E) is provided. Data from the UK wells include depths, and WSM-type quality ranking. The ranking for the two analysed wells 3/15-9a and 3/15-10 is B and D (Tab. 1). However, given the low circular standard deviation ($< 15^\circ$) and the similar σ_H orientations to 3/15-10, the orientation of 3/15-9a can be considered reliable.

TABLE 1: Combined (BO and DIF) circular parameters and quality ranking for data in the UK sector. BO = breakout; L = length; var = variance; s.d. = standard deviation; Q = quality ranking.

Well	Lon [$^\circ$]	Lat [$^\circ$]	Top - Base BO Depth [m]	No. of BO	No. of DIFs	Total SFI L [m]	Circular var [$^\circ$]	Circular s.d. [$^\circ$]	Average σ_H Orientation [$^\circ$]	WSM Q
3/15-9a	1.8354	60.5123	3728 - 3785	13	2	9.11	4.84	12.03	90.87	D
3/15-10	1.9006	60.5446	3587 - 3951	10	27	41.42	2.73	8.95	91.42	B

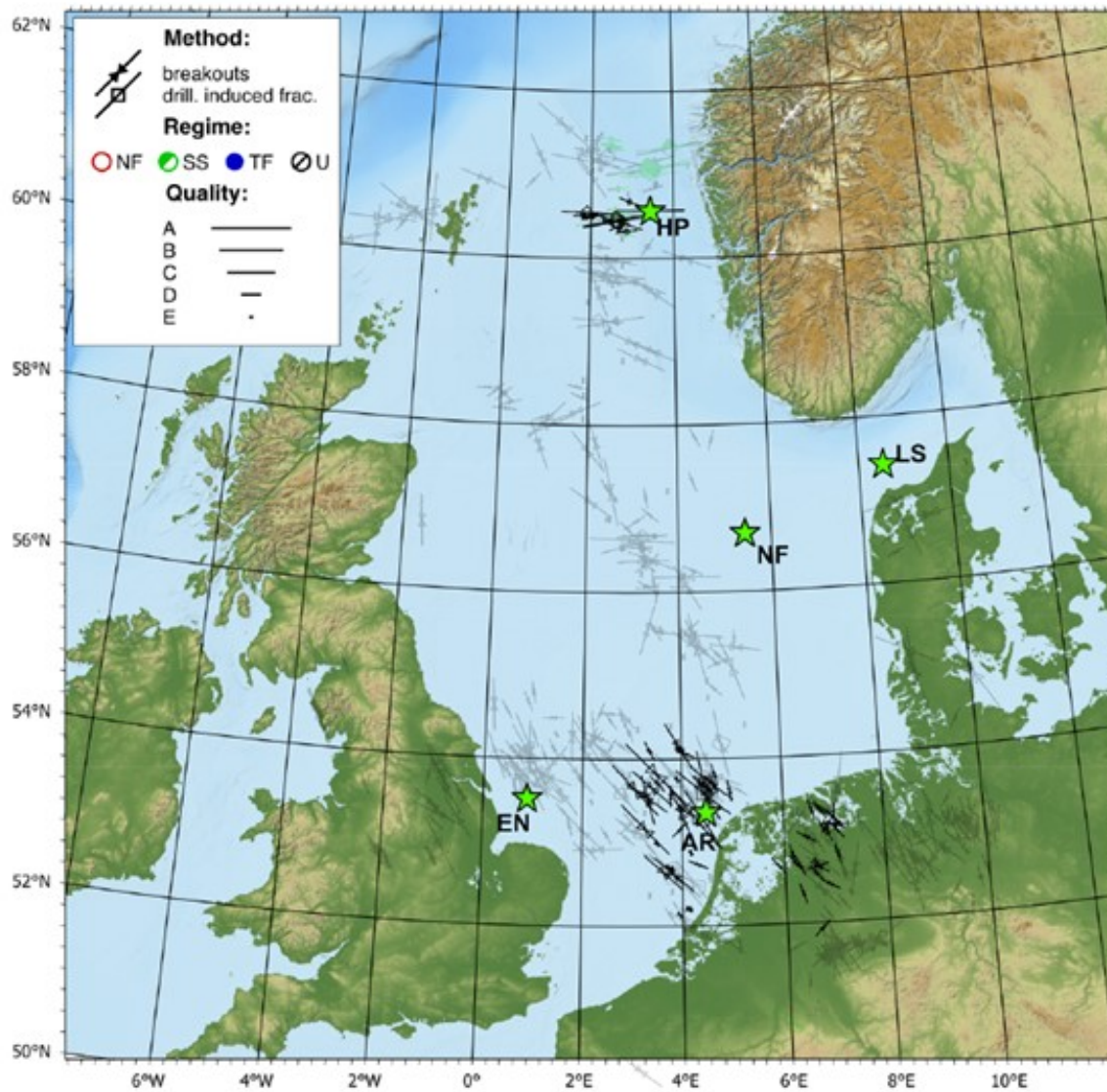


FIGURE 21: Plot of new borehole stress orientation measurements from D2.2 (in black) and the existing WSM2016 data (in light grey) for comparison. Symbol size is proportional to quality. NF = Normal faulting; SS = Strike-slip; TF = thrust faulting and U = unknown; AR = Aramis area; NF = Nini Field; LS = Lisa Structure; HP = Horda platform. A dominant NW-SE σ_H is observed in the Dutch and UK sectors, whereas an E-W σ_H predominates near the Horda Platform.

2.2.3 The updated focal mechanisms catalogue and additional moment tensor solutions

The updated focal mechanisms catalogue follows the typical convention of describing focal mechanism by the strike, dip and rake of one of the focal planes. The principal stress axis orientations (trends and plunges of σ_V , σ_H and σ_h) can be calculated from the above. The updated focal mechanisms catalogue does not include quality of the focal mechanisms since only NNSN reported quality for their events (10 events with A- and B-qualities). However, quality control was somewhat achieved by including exclusively high-quality data (events after the year 1980); further details in D2.4. Therefore, focal mechanisms from the WSM2016 were not included in the updated catalogue since in the WSM2016 single focal mechanism solutions (FMS) are never ranked higher than 'C'.

The updated focal mechanism catalogue contains 70 entries describing presumably 54 (or 55) individual events, and only one of these events occurs between latitude 60° and 61° within the Horda Platform (no. 65 in Fig. 22). The accuracy of the reported event depth cannot be granted since this depends on a number of factors including number and distance of stations recording each event, station azimuthal gap (the largest angle without a seismic station) etc. Additionally, event depths of 10 or 15 kilometres in catalogues may not accurately represent the true event depths, instead they could be standardised values utilised for calculating the mechanism in cases where no depth estimation was provided.

Therefore, as part of the Deliverable 2.4, for seven selected events having the best station distribution and data quality, moment tensor solutions were computed using a probabilistic approach for the moment tensor estimation, which also allow for depth estimations and location uncertainties. In certain cases, where focal mechanisms have already been reported in literature, a comparison between the solutions of focal mechanisms and depth estimates has been also provided in D2.4 (Section 5). None of these FMSs occurs between latitude 60° and 61° within the Horda Platform (see red focal mechanisms in Fig. 23).

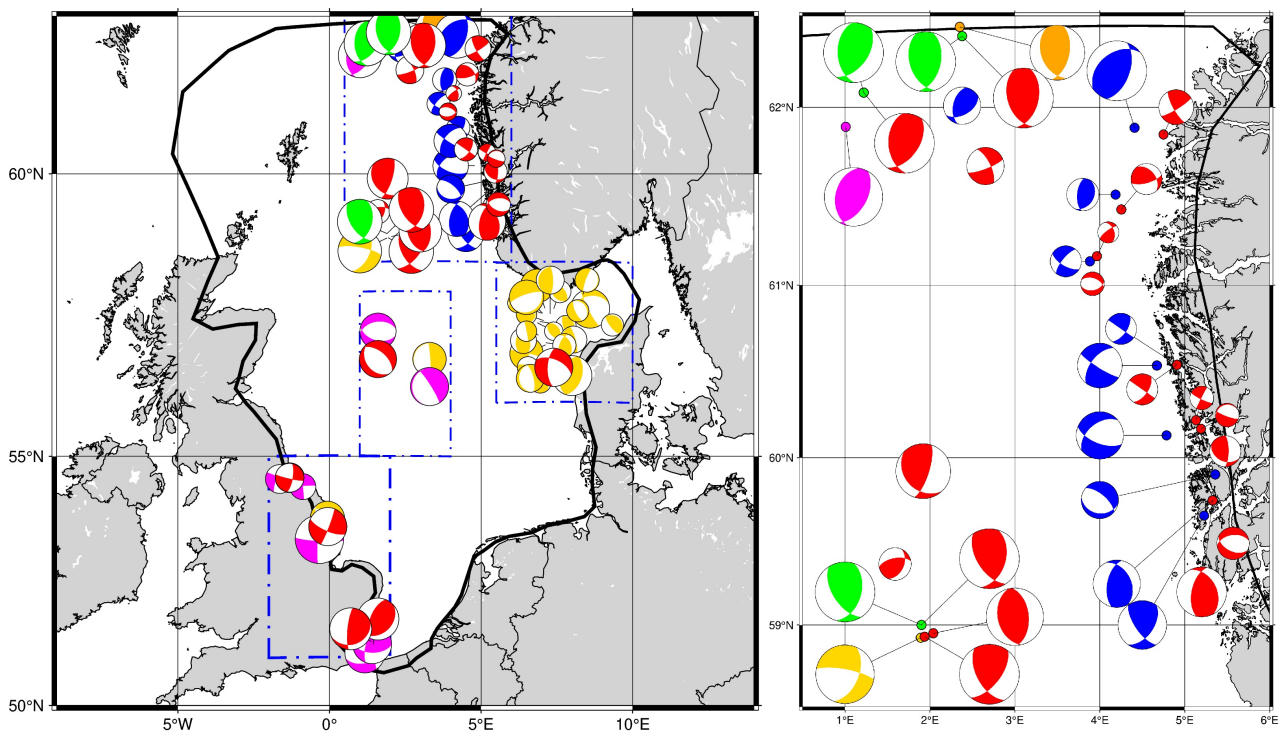


FIGURE 22: (left) Focal mechanism catalogue for the North Sea area. Focal mechanism size is proportional to event magnitude. Blue rectangles denote regions presented in more detail in D2.4 and not shown here. (right) Close up of the focal mechanism catalogue for the Norwegian west coast. Colours mark reporting institutions: green = GCMT, red = ISC, yellow = GEUS, blue = NNSN, orange = GEOFON.

2.3 Data integration

The location of the numerical geomechanical Smeaheia model is presented in Fig. 23. Due to the very limited number of focal mechanisms within this region, in this synthesis we covered a larger area

between longitude 0°-6°E and latitude 58°-62.5°N (blue box in Fig. 23), since this region covers both the full extent of the Horda Platform (pink region in Fig. 23) and Viking Graben (purple region in Fig. 23). An overview of all stress data and information used in this report are shown in Tab. 2.

TABLE 2: Overview of the stress data; FMS = earthquake focal mechanisms data, DIF: = drilling-induced tensile fracture; BO = borehole data; OC = overcoring; Note that WSM2016 quality depends on the data type (see text) and that the quality-ranking by Equinor differs from WSM2016. no./No. = number of data over the total.

Database	Type	σ_1 (no./No.)	σ_2 (no./No.)	σ_3 (no./No.)	AZI (no./No.)	Quality
WSM2016	FMS	37/37	36/37	36/37	32/37	27C; 5D; 5E
WSM2016	DIF	x	x	x	38/42	3A; 8B ;5C ;16D; 10E
WSM2016	BO	x	x	x	32/68	3B; 17C; 10D; 38E
WSM2016	OC	2/2	2/2	2/2	2/2	2D
SHARP	updated FM catalogue	70/70	70/70	70/70	x	x
SHARP	re-computed FMS	3/3	3/3	3/3	x	x
SHARP	new BO data - Equinor	x	x	x	11/11	3B; 1C; 6D; 1E;
SHARP	new BO data - BGS	x	x	x	2/2	1B; 1D

In Fig. 23, all existing stress data for the region are reported independently of their quality, while in Fig. 24 we exclusively show WSM2016 data with quality A-B. Although large uncertainties in the azimuth of the σ_H from the WSM2016 with low quality exist, the overall azimuth is rather consistent within the area (Fig. 23). Focal mechanisms from the updated catalogue are shown in blue, while the newly computed focal mechanisms in red in Fig. 23. Of the seven computed focal mechanisms, three events (no.3: 16 October 2014, no.5: 30 June 2017 and no.7: 21 March 2022) have their best relocation (best computed FMS) in the region between longitude 0°-6°E and latitude 58°-62.5°N (blue outline in Figs. 23 and 24).

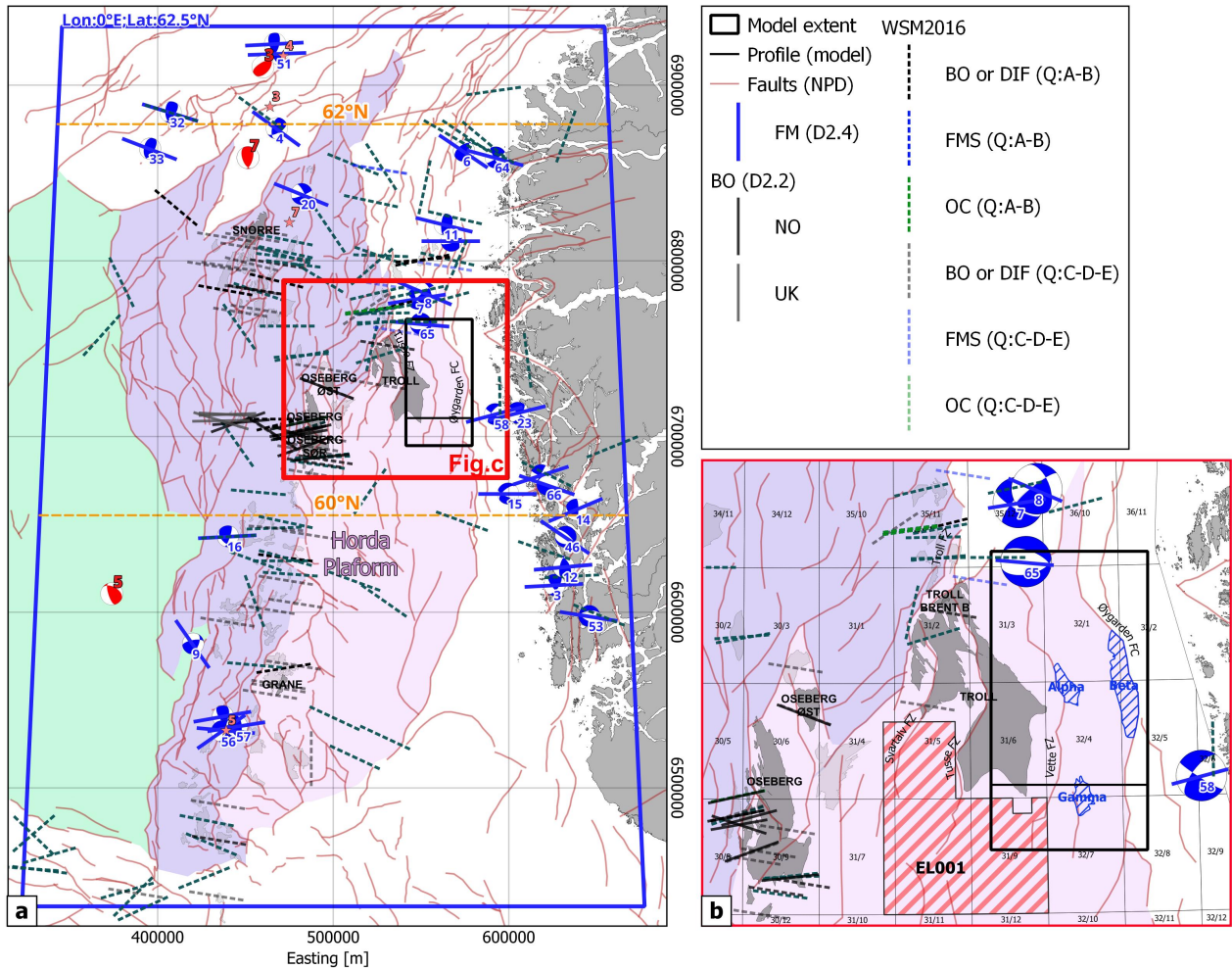


FIGURE 23: Overview of the stress data for a region between longitude 0°-6°E and latitude 58°-62.5°N (blue outline). The location of the Horda Platform, Viking Graben and Shetland Platform are shown as purple, pink and green regions. The location of oil field are shown in light grey and the Troll, Oseberg and Snorre fields in dark grey. Fault traces are reported as red lines. Region extent, oil field and fault traces are from the Norwegian Offshore Directorate, NOD). (a) Stress data from WP2 are presented as: (i) blue focal mechanisms and azimuth of the σ_H (blue lines) for the updated FM catalogue, (ii) azimuth of the σ_H (black and grey lines) for the additional borehole stress observation and (iii) azimuth σ_H (dashed lines, colour-coded by type and quality) for the existing WSM2016. The newly-computed moment tensor solutions are reported as red focal mechanisms. The extent of the geomechanical Smeaheia model and the location of the E-W profile are shown as black box outline and horizontal line, respectively. (b) Close-up of map a, including also the licence blocks, the exploitation licence EL001, and the location of Alpha, Beta and Gamma prospects.

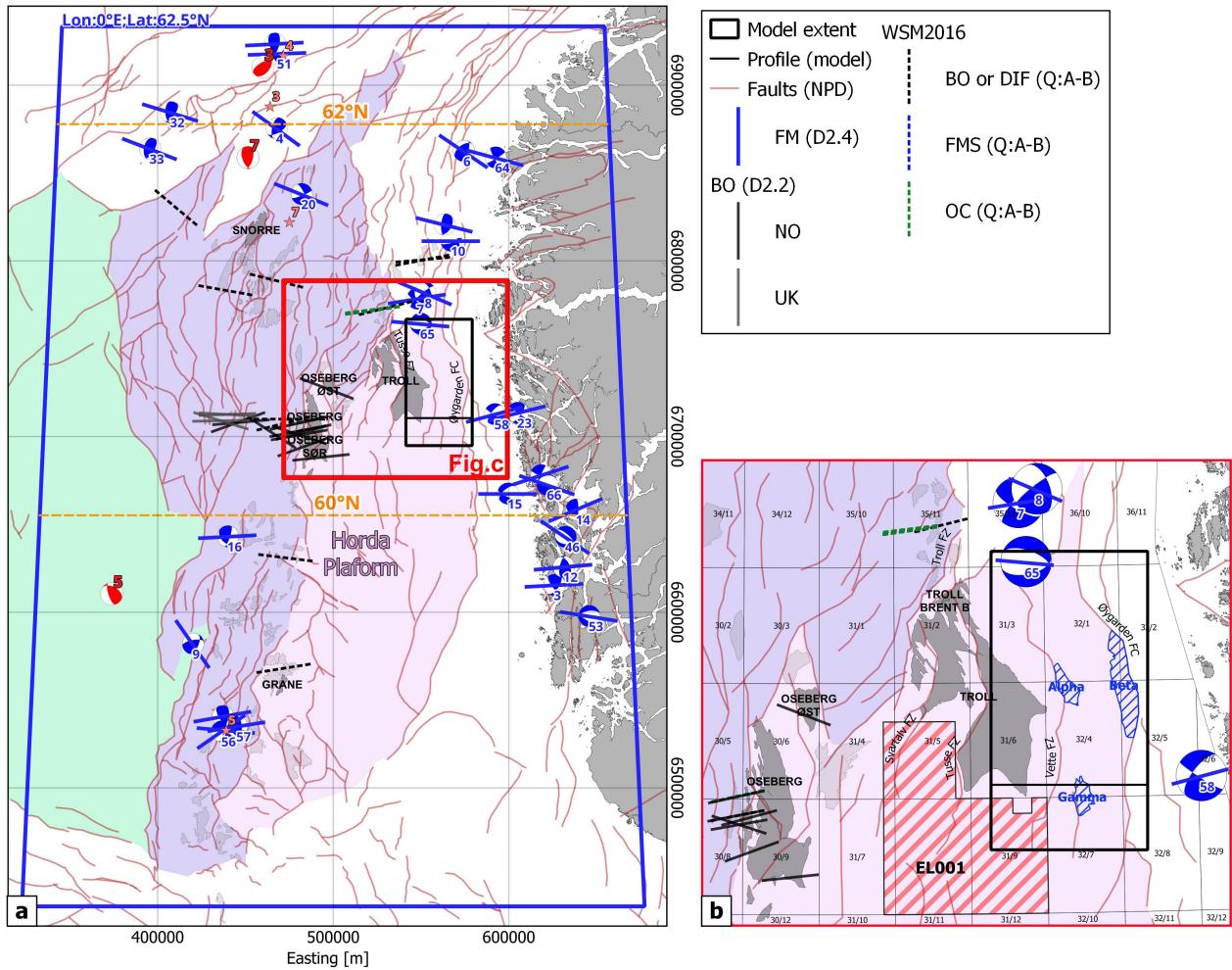


FIGURE 24: Same of Fig. 23, but including only WSM2016 stress data with A- and B-quality.

In order to compare stress data from focal mechanisms and boreholes, we have derived the P-, B- and T-axes (pressure, null and tension, respectively) from the focal mechanisms as proxy for the orientation of the principal stress axes (σ_1 , σ_2 and σ_3 , respectively). Although stress magnitude cannot be determined from focal mechanisms, it is possible, based on the stress axes plunges (or by the definition of the stress regime), to determine which stress axis is the vertical, and by indexing of the stress axes determine which one of the remaining stress axes is the σ_H and which one σ_h . However, focal mechanism alone do not provide information on stress magnitude. Consequently, it is not possible to determine if the stress is horizontally isotropic ($\sigma_H = \sigma_h$), indicating some potential limitations to this approach.

The updated focal mechanism catalogue comprises six focal mechanisms located within the Viking Graben (purple in Fig. 25), one within the Horda Platform (pink in Fig. 25) and one further west in the Shetland Platform (green in Fig. 25). Furthermore, focal mechanisms no. 7, no. 8, no. 10, and no. 11 are situated at approximately the same longitudes as the numerical geomechanical Smeaheia model, up to about 50 km north of its northern edge, while no. 58 is located roughly 13 km east of the model's eastern edge.

The newly computed moment tensor solutions using a probabilistic approach comprises seven focal mechanisms, four of them are located outside the analysed area, one of them is relocated within the Shetland Platform and two are within the analysed area, but outside the Horda Platform, Viking Graben and Shetland Platform areas (Fig. 23 and Fig. 27). The closest FM to the the numerical geometrical Smeaheia model is no. 7, located at circa 128 km to the NW.

For completeness, we also determined the orientation of the principal stress axes (σ_1 , σ_2 and σ_3) for the FMSs and OCs data from the WSM2016, although the poorer quality. Eight and two FMSs occur respectively within the Viking Graben and Horda Platform (purple and pink FMs in Fig. 26). The empty focal mechanism represent a data for which only the orientation of two of the principal stress axes are reported in the WSM2016 ('wsm11536'), and since it had the poorest quality ('E'), we did not plot it.

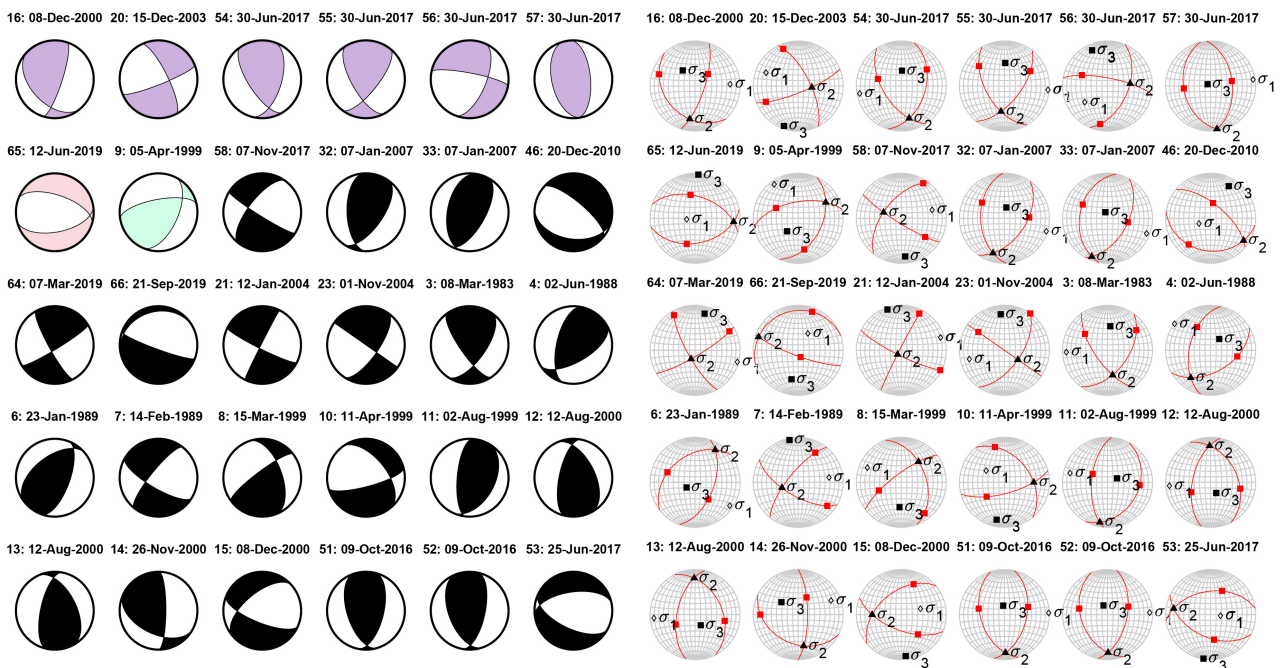


FIGURE 25: Stress data from the updated focal mechanisms catalogue for the blue outlined region shown in Fig. 23, shown as (left) focal mechanisms and (right) equal area lower hemisphere stereonets with focal planes (red great circles), slip vectors (red squares) and principal stress axes. The focal mechanisms are colour-coded by location: purple for the Viking Graben, pink for the Horda Platform, green for the Shetland Platform or black for none of the above locations. The catalogue IDs and date of the event are reported.

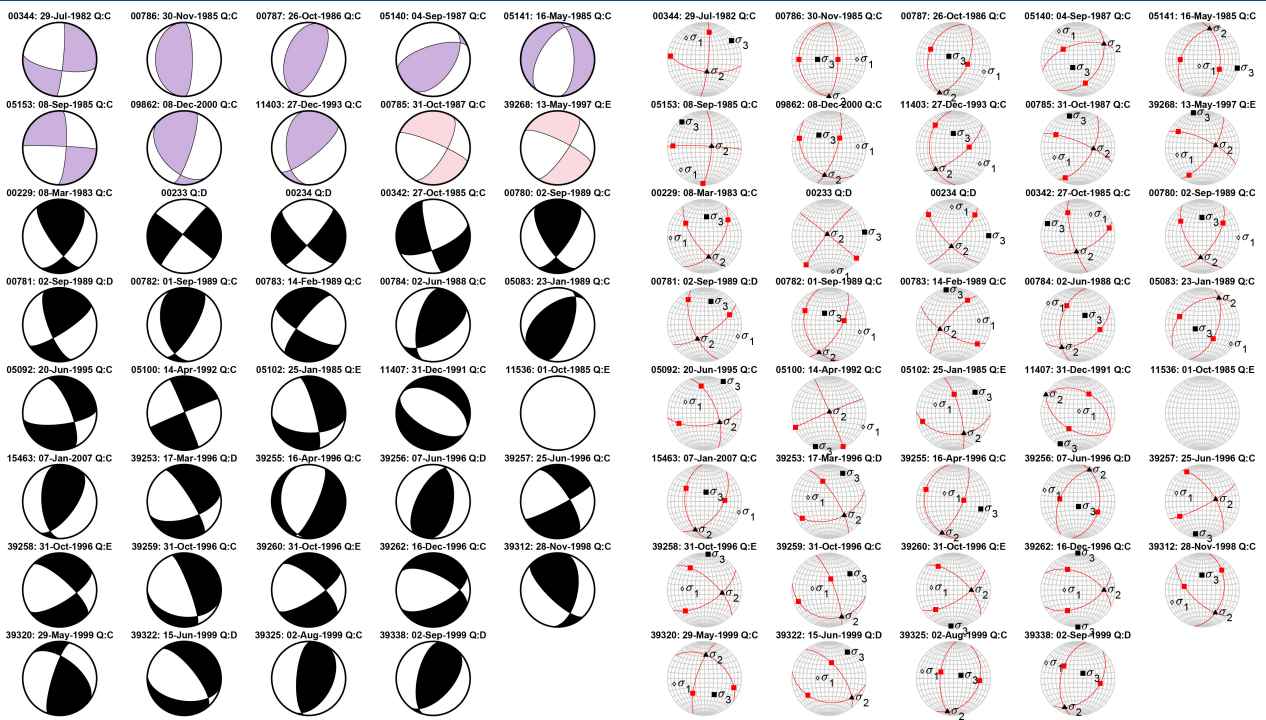


FIGURE 26: Stress data from the WSM2016 for the blue outlined region shown in Fig. 23, shown as (left) focal mechanisms and (right) equal area lower hemisphere stereonets with focal planes (reg great circles), slip vectors (red squares) and principal stress axes. The focal mechanisms are colour-coded by location: purple for the Viking Graben, pink for the Horda Platform, green for the Shetland Platform or black for none of the above locations. The WSM2016 Ids (exclusive of 'wsm') and date of the event are reported.

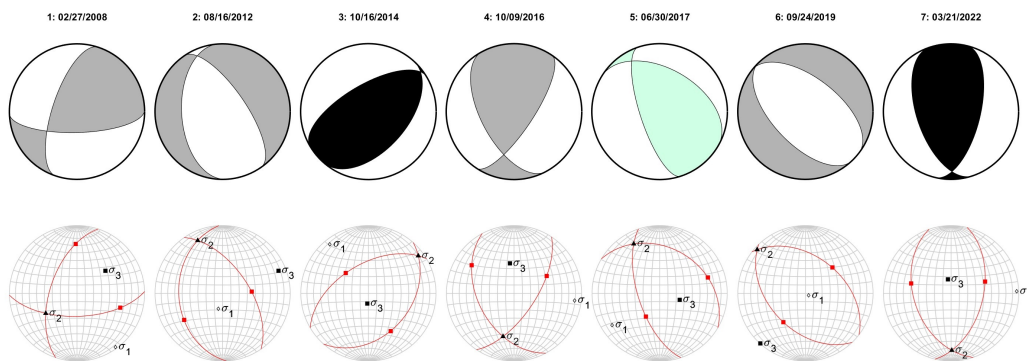


FIGURE 27: Newly-computed FMSs, shown as (top) focal mechanisms and (bottom) equal area lower hemisphere stereonets with focal planes (reg great circles), slip vectors (red squares) and principal stress axes. The focal mechanisms are colour-coded by location: purple for the Viking Graben, pink for the Horda Platform, green for the Shetland Platform. Black for none of these three locations, but still within the analysed region (blue outlined region shown in Fig. 23) while grey for FMSs outside the analyzed region.

Some of the FMs in the updated focal mechanism catalogue (Fig. 25) are also reported in the WSM2016 (Fig. 26); There is not substantial difference in the FMs solution, but the location differs for some of

these. Below are listed the events that are in both catalogues for analyzed region:

- no.3 = wsm00229; Date: 08 March 1983; WSM16 Quality = C; Location Distance: ~11 km;
- no.4 = wsm00784; Date: 02 June 1988; WSM16 Quality = C; Location Distance: ~13 km;
- no.6 = wsm05083; Date: 23 January 1989; WSM16 Quality = C; Location Distance: ~9 km;
- no.7 = wsm00783; Date: 14 February 1989; WSM16 Quality = C; Location Distance: ~4 km;
- no.16 = wsm09862; Date: 08 December 2000; WSM16 Quality = C; Location Distance: 0 km;
- no.32 = wsm15462; Date: 07 January 2007; WSM16 Quality = C; Location Distance: 0 km;

The best quality reported in the existing WSM2016 for FMs is C. For C-quality, only three out of 26 data have the vertical axis corresponding to σ_1 as we would expect from normal stress regime (Fig. 28). The only data located in the Viking Graben is one of these events. Reverse $\sigma_v \equiv \sigma_3$ to strike slip $\sigma_v \equiv \sigma_2$ regimes are dominating in and outside the Horda Platform and Viking Graben areas.

The maximum horizontal stress azimuth (AZI and σ_H azimuth from the WSM2016) show progressively more scattering as data quality reduces (Fig. 29). However, a dominating E-W azimuth is still observed.

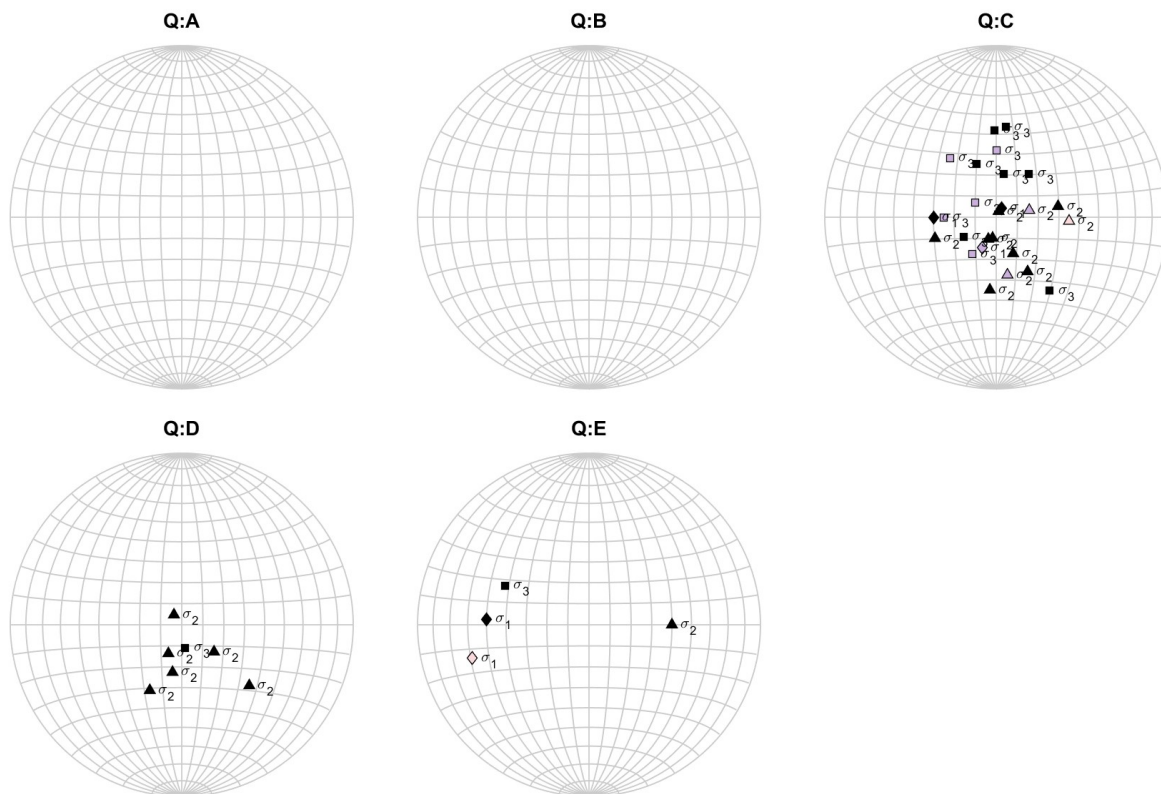


FIGURE 28: WSM2016 σ_V -derived stress axis plotted on equal area lower hemisphere stereonets, depending on quality (Q). Purple symbols are for the Viking Graben, pink symbols for the Horda Platform, green symbols for the Shetland Platform and black symbols are outside of the above mentioned regions. Diamond symbols indicate $\sigma_V \equiv \sigma_1$, triangle for $\sigma_V \equiv \sigma_2$ and square for $\sigma_V \equiv \sigma_3$

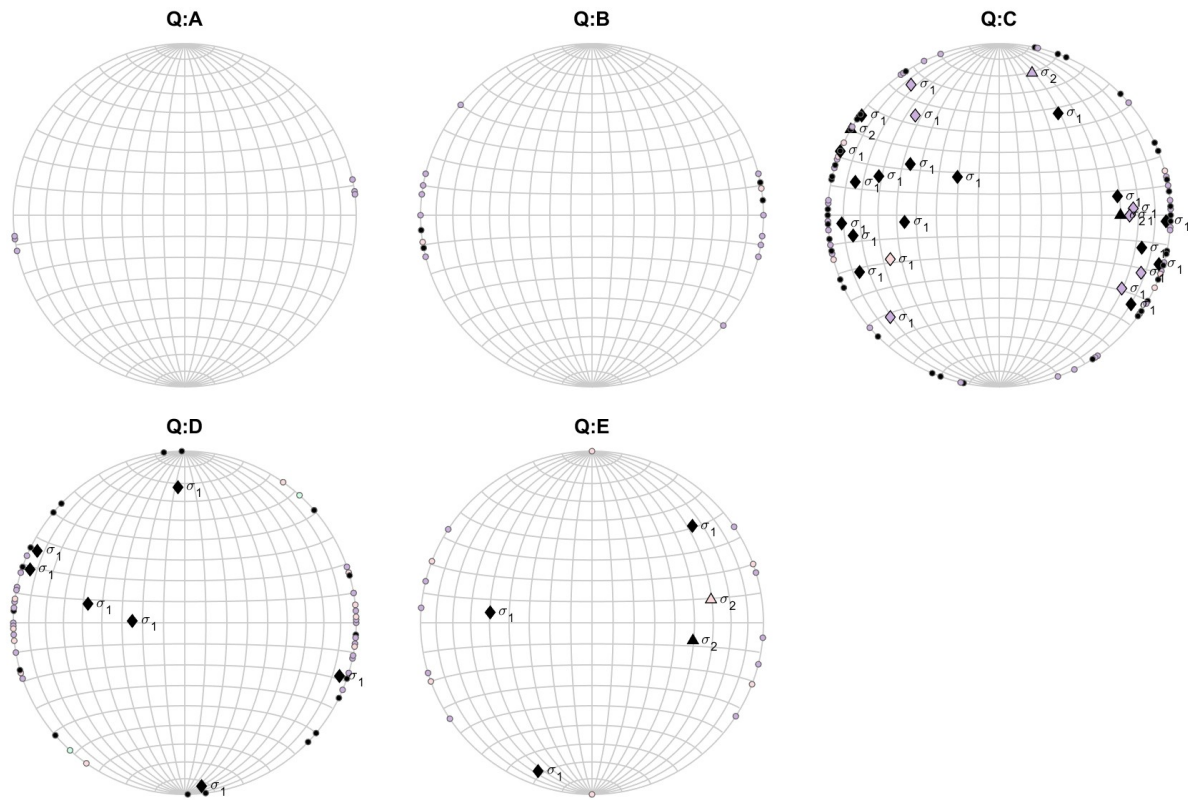


FIGURE 29: WSM2016 σ_H -derived stress axis plotted on equal area lower hemisphere stereonets depending on quality (Q). Furthermore AZI($\pm 180^\circ$) data from the WSM2016 are plotted on equal area lower hemisphere stereonets, depending on quality. Purple symbols are for the Viking Graben, pink symbols for the Horda Platform, green symbols for the Shetland Platform and black symbols are outside of the above mentioned regions. Diamond symbol for σ_1 , triangle for σ_2 and square for σ_3 .

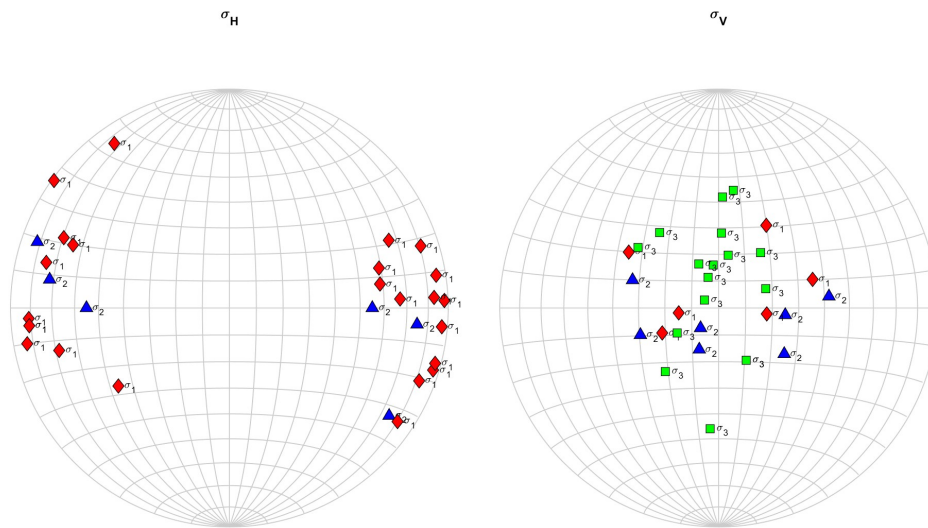


FIGURE 30: (left) σ_H and (right) σ_V from the updated focal mechanism catalogue, plotted on equal area lower hemisphere stereonets. σ_1 are shown as red diamonds, σ_2 as blue triangles and σ_3 as green square symbols.

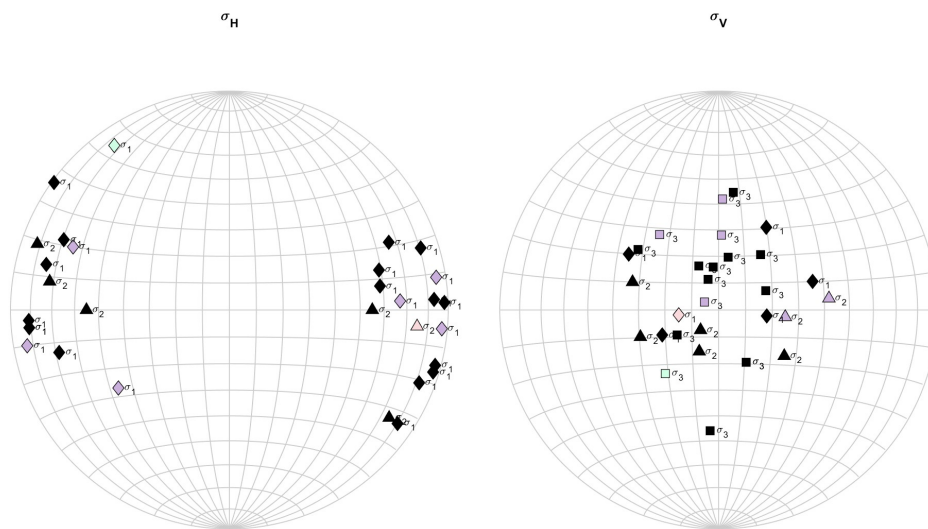


FIGURE 31: (left) σ_H and (right) σ_V from the updated focal mechanism catalogue, plotted on equal area lower hemisphere stereonets. σ_1 are shown as diamonds, σ_2 as triangles and σ_3 as square symbols and colour-coded by location. Purple symbols are for the Viking Graben, pink symbols for the Horda Platform, green symbols for the Shetland Platform and black symbols are outside of the above mentioned regions.

In Fig. 30, we plotted σ_H and σ_V derived from the updated catalogue of focal mechanisms. Focal mechanisms have large majority (24/30) of $\sigma_H \equiv \sigma_1$ and large majority (17/30) of $\sigma_V \equiv \sigma_3$, which suggest an overall reverse stress regime. However, the focal mechanism from the Horda Platform

(no. 65), indicates normal stress regime ($\sigma_V \equiv \sigma_1$, Fig. 31). For this event, zero depth is reported in the catalogue.

In Fig. 32, we plotted σ_H and σ_V derived from the newly-computed focal mechanisms. σ_H orientation is rather scattered but majority (5/7) of $\sigma_V \equiv \sigma_3$, which suggest an overall reverse stress regime. None of the computed FMSs is located within the Horda Platform nor Viking Graben. The closest FMS to the Viking Graben (no. 7), indicates reverse regime ($\sigma_V \equiv \sigma_1$ with E-oriented σ_H Fig. 33).

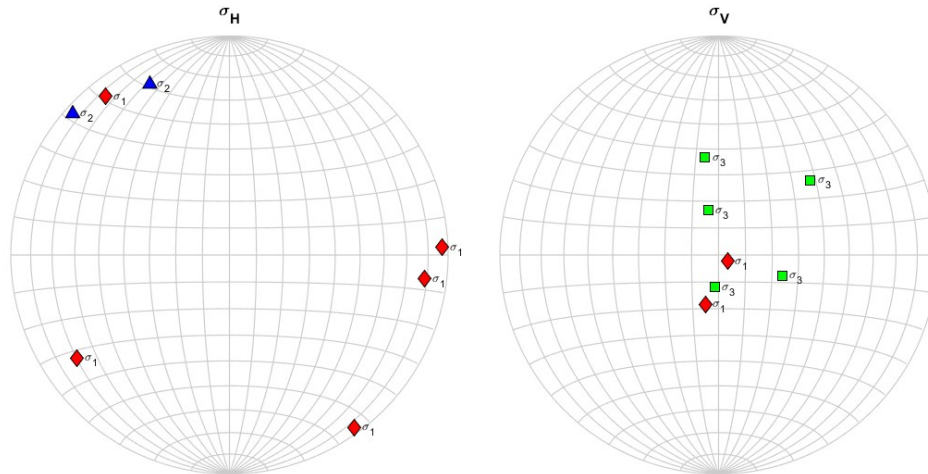


FIGURE 32: (left) σ_H and (right) σ_V from the newly-computed FMSs, plotted on equal area lower hemisphere stereonets. σ_1 are shown as red diamonds, σ_2 as blue triangles and σ_3 as green square symbols.

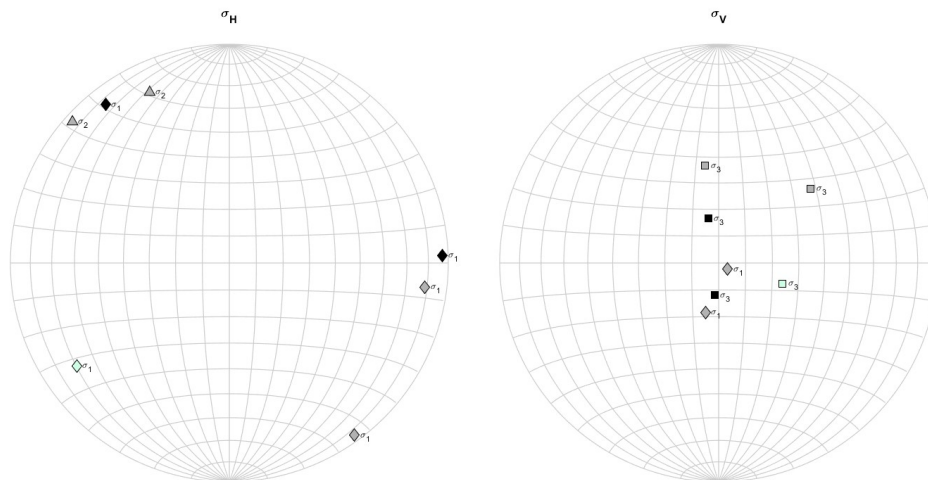


FIGURE 33: (left) σ_H and (right) σ_V from the newly-computed FMSs, plotted on equal area lower hemisphere stereonets. σ_1 are shown as diamonds, σ_2 as triangles and σ_3 as square symbols and colour-coded by location. Purple symbols are for the Viking Graben, pink symbols for the Horda Platform, green symbols for the Shetland Platform and black symbols are outside of the above mentioned regions.

Since the final aim of this stress integration is to inform the Numerical Geomechanical Smeaheia

Model at local- and crustal-scale, we present the horizontal stress azimuths (σ_H and σ_h) as function of depth in Fig. 34 left. The plotted data include high-quality (A- and B-rated) data from the World Stress Map 2016 (WSM2016) alongside maximum and minimum principal horizontal stress azimuths (σ_H and σ_h) derived from updated focal mechanisms catalogue and additional FMSs, and the borehole observations provided by Equinor and BGS. The quality of the WSM2016 and borehole data is depicted with error bars, and an arbitrary error value of 50° is assigned for E-quality data, reflecting its larger uncertainty ($>40^\circ$). We use the WSM2016 quality ranking values to also display error-bars for the Equinor data. Furthermore, since not all data from Equinor provided with top and bottom failure depth, for the data lacking these depth, we plotted borehole depths to have approximate depth estimation.

Equinor provided data for a broader region beyond the $60\text{-}61^\circ$ Northing range presented in D2.2. Consequently, we included all data for the analysed region (indicated by the blue outline in Fig. 23) to provide a comprehensive overview. These data are plotted in semi-transparent orange colour as opposite to the reported data in full-opaque orange colours (Fig. 34).

To compare all stress data with maximum horizontal stress (σ_H), we included the mean azimuth and standard deviation ($90.9^\circ \pm 21.3^\circ$) used in the probabilistic fault stability assessment (D5.4) (blue vertical line and shaded blue regions Fig. 34). The inferred σ_h , orthogonal to σ_H , is also shown with light blue shaded regions.

Stress data do not reveal any clear trend or rotation of maximum horizontal stress azimuth with depth (Fig. 34 left, also considering the depth uncertainties associated with the FMs. Although the large depth uncertainties associated with these data, the focal mechanisms in the updated FM catalogue which are closest to the model (no. 7, 8, 10, 11 and 65) are within the standard deviation for the azimuth of σ_H used for the probabilistic fault stability assessment (D5.4), supporting that using these values is a reasonable assumption. Furthermore, the newly-computed focal mechanism closed to the Viking Region areas (no. 7) show a consistent σ_H orientation and indicates reverse stress regime at depth of approximately 15 km (black dot in Fig. 34).

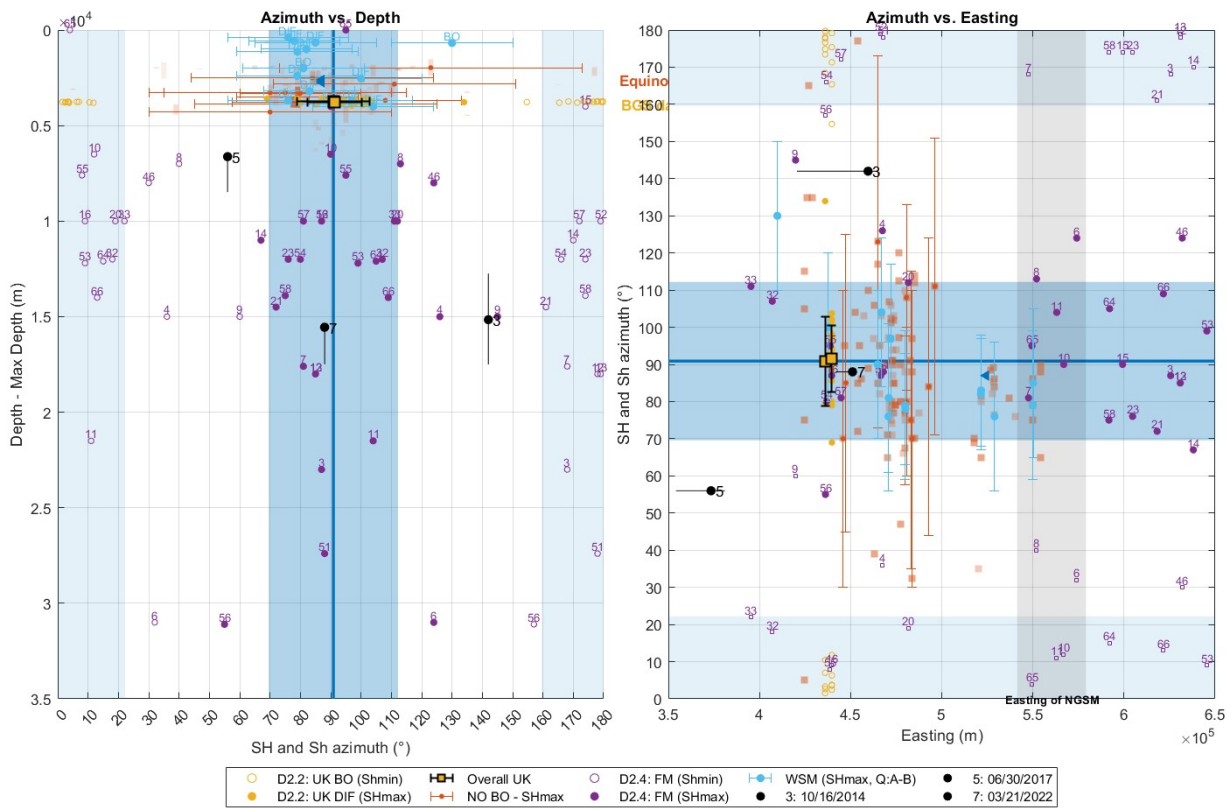


FIGURE 34: Overview of the maximum and minimum principal horizontal stress orientation collected during the SHARP and existing data in the WSM2016 plotted as function of (left) depth and (right) Easting. Filled and hollow symbols correspond to the σ_H and σ_h . Borehole data collected within SHARP are displayed in yellow (BGS data) and orange (Equinor data), while borehole data are displayed in purple. The top depth of the reservoir at the EOS well in a and its location (Easting) are indicated by the blue triangle. Mean azimuth and standard deviation used in the probabilistic fault stability assessment are represented as blue line and shaded blue region, while the inferred σ_h as light blue shaded regions. Shaded grey region indicates the Easting of the Numerical Geomechanical Smeaheia Model (NGSM).

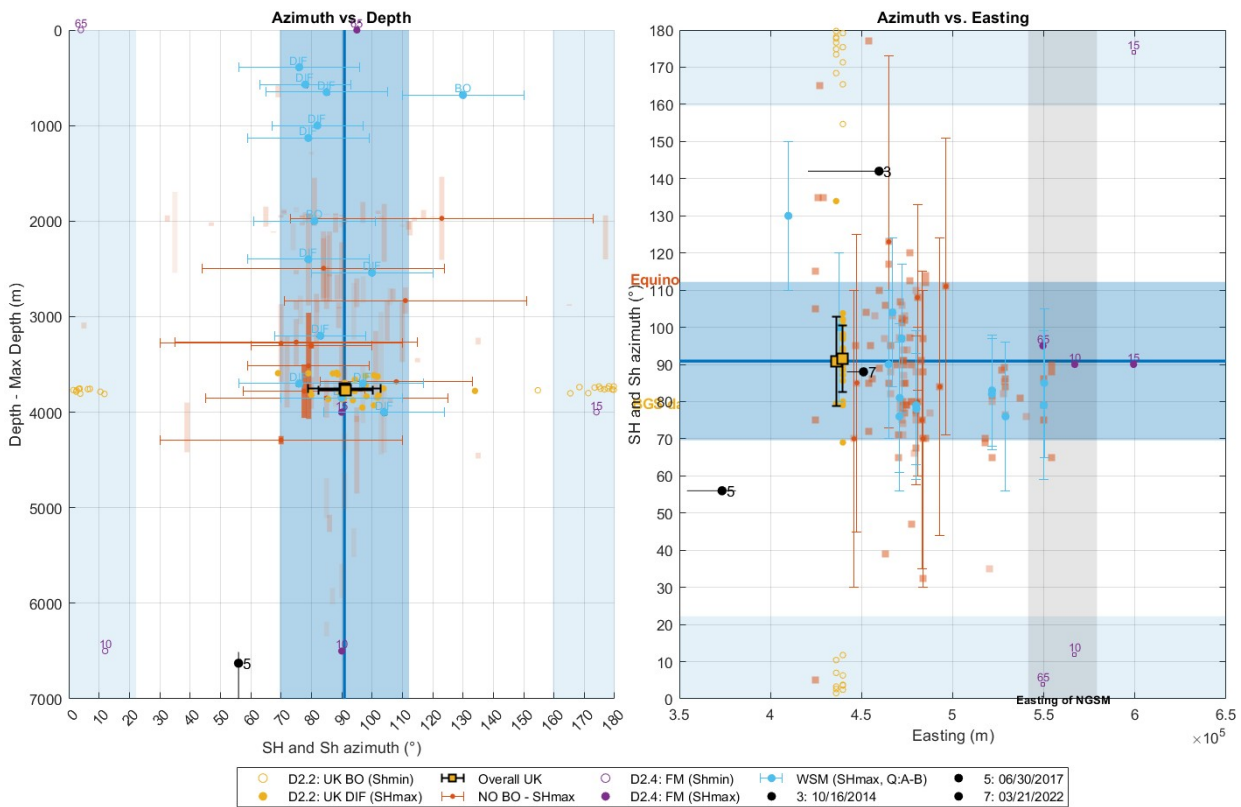


FIGURE 35: Same of Fig. 34, but only focusing on the shallower 7000 m.

At shallow depths (below 4000 m), WSM2016 data with high quality consist of DIFs and BOs. Fig. 35 left focuses depth <7000 m, and large majority of the data falls within the mean and standard deviation values used in the probabilistic fault stability assessment. This also applies to the new BO data provided by Equinor and BGS (orange and yellow data points in Fig. 35). Shallower (<7000 m depth) focal mechanisms in the updated FM catalogue (no. 10 and no. 15) have a E-W σ_H and normal stress regime.

Furthermore, we plotted the same data as function of Easting (Figs. 34 right and 35 right, considering that long-lived structures in the northern North Sea are mostly N-S striking. The σ_H and σ_h in function of Easting plot reveals small azimuthal rotation with reducing angles from circa $90^\circ \pm 20^\circ$ between 430000 km Easting to circa $80^\circ \pm 20^\circ$. This azimuthal rotation is depicted by the shallow stress data (existing BO and DIF data from the WSM2016 and the new data provided by Equinor and BGS) but cannot be confirmed through FMSs. Although it based on a limited amount of data East of 500000 m, this azimuthal rotation could be related to structural control of the stress. Interestingly, the Numerical Geomechanical Smeaheia Model (NGSM) lies to the East of the above mentioned transition (grey region in Fig. 34 right).

2.4 Concluding remarks

In this section, we have attempted to integrate diverse types of in-situ stress data observations in a cohesive framework to inform the Numerical Geomechanical Smeaheia Model (D1.5). Given the limited seismic activity in the Horda Platform region, which has constrained the availability of good-quality data for computing Fault Mechanism Solutions (FMSs), we extended our analysis to a broader

geographic area (blue outline in Fig. 23). This approach allowed us to incorporate deep-seated information from FMSs. The disparity in the volume of available data — specifically, the greater number of borehole measurements compared to focal mechanisms — introduces larger uncertainties regarding in-situ stress at depth. Although focal mechanisms offer valuable insights, the extension of our analysis to a wider area introduces potential noise, and the depth of events, for which focal mechanisms are computed, cannot always be reliably ascertained due to missing station coverage and large station-event distances. When interpreting the data, this aspect needs to be accounted for.

Our integration reveals a generally consistent orientation of the principal maximum horizontal stress (σ_H), aligning well with the values used in the Probabilistic Fault Stability Assessment. This consistency holds true for shallow-depth observations and for focal mechanisms in general. Despite the expected variability in the azimuth of σ_H from focal mechanisms (given the large analysed region), the six focal mechanisms from the updated focal mechanism catalogue that occur nearby the Horda Platform (nos. 7, 8, 10, 11, 58, and 65, indicated by purple dots in Fig. 34) and the one newly computed focal mechanism located in the Viking Graben (no. 7. black dot in Fig. 34) are within the standard deviation values used in the Probabilistic Fault Stability Assessment.

To improve data reliability and depth information, an increase in the number of seismic stations in proximity to events is recommended. This would enhance data quality and facilitate the computation of more reliable focal mechanism solutions, similar to the seven newly computed focal mechanisms presented in deliverable D2.4: "Updated catalog and focal mechanism database". Since the moment tensor inversion was performed probabilistically, these solutions incorporate uncertainties and quality metrics, which are often overlooked by reporting institutions, but are crucial for accurate interpretations. Furthermore, a larger number of seismic stations is also beneficial to other type of analyses (including stress drop) that would bring additional valuable information to this in-situ stress integration.

While a minor azimuthal rotation of σ_H cannot be completely ruled out, it cannot be confirmed based solely on the available focal mechanism data due to the aforementioned limitations and uncertainties in depth.

Due to the limited data available, we are unable to definitively characterise the prevailing stress regime at both shallow and crustal depths within the Horda Platform. Borehole information from WSM2016 and other borehole observations only provided azimuths for σ_H , while Fault Mechanism Solutions (FMSs) indicate stress regimes. However, the current lack of good quality FMS for the Horda Platform and the unreliable depth information for the existing ones, makes FMSs unsuitable for this purpose.

In contrast, outside the Horda Platform, where a more extensive dataset is available, the updated focal mechanism catalogue indicates a predominantly reverse stress regime with an E-W maximum horizontal stress azimuth (Fig. 30). This finding is also consistent with the few newly computed focal mechanisms (Fig. 32).

References

- Allmann, Bettina P and Peter M Shearer (2007). "Spatial and temporal stress drop variations in small earthquakes near Parkfield, California". In: *Journal of Geophysical Research: Solid Earth* 112.B4.
- Brune, James N (1970). "Tectonic stress and the spectra of seismic shear waves from earthquakes". In: *Journal of geophysical research* 75.26, pp. 4997–5009.
- Eshelby, John Douglas (1957). "The determination of the elastic field of an ellipsoidal inclusion, and related problems". In: *Proceedings of the royal society of London. Series A. Mathematical and physical sciences* 241.1226, pp. 376–396.
- Goertz-Allmann, Bettina P, Benjamin Edwards, Falko Bethmann, Nicholas Deichmann, John Clinton, Donat Fäh, and Domenico Giardini (2011). "A new empirical magnitude scaling relation for Switzerland". In: *Bulletin of the Seismological Society of America* 101.6, pp. 3088–3095.
- Grünthal, Gottfried, Rutger Wahlström, and Dietrich Stromeyer (2009). "The unified catalogue of earthquakes in central, northern, and northwestern Europe (CENEC)—updated and expanded to the last millennium". In: *Journal of Seismology* 13, pp. 517–541.
- Hanks, Thomas C and David M Boore (1984). "Moment-magnitude relations in theory and practice". In: *Journal of Geophysical Research: Solid Earth* 89.B7, pp. 6229–6235.
- Hanks, Thomas C and Hiroo Kanamori (1979). "A moment magnitude scale". In: *Journal of Geophysical Research: Solid Earth* 84.B5, pp. 2348–2350.
- Heidbach, O, Andreas Barth, Birgit Müller, John Reinecker, Ove Stephansson, Mark Tingay, and A Zang (2016a). *WSM quality ranking scheme, database description and analysis guidelines for stress indicator*. Tech. rep. GFZ German Research Centre for Geosciences.
- Heidbach, Oliver, Mojtaba Rajabi, Karsten Reiter, Moritz Ziegler, Wsm Team, et al. (2016b). "World stress map database release 2016". In: *GFZ Data Services* 10, p. 1.
- Mykkeltveit, S. and F. Ringdal (1981). "Phase identification and event location at regional distance using small-aperture array data". In: *Identification of Seismic Sources—Earthquake or Underground Explosion: Proceedings of the NATO Advance Study Institute held at Voksenåsen, Oslo, Norway, September 8–18, 1980*. Springer, pp. 467–481.
- Prieto, German Andrés, RL Parker, and FL Vernon Iii (2009). "A Fortran 90 library for multitaper spectrum analysis". In: *Computers & Geosciences* 35.8, pp. 1701–1710.
- Shearer, Peter M, Germán A Prieto, and Egill Hauksson (2006). "Comprehensive analysis of earthquake source spectra in southern California". In: *Journal of Geophysical Research: Solid Earth* 111.B6.
- Thompson, N., J. S. Andrews, L. Wu, and R. Meneguolo (2022). "Characterization of the in-situ stress on the Horda platform - A study from the Northern Lights Eos well". In: *International Journal of Greenhouse Gas Control* 114, p. 103580.